Evaporation-induced flow around a droplet in different gases

S. Radhakrishnan, T. N. C. Anand,* and Shamit Bakshi†

Department of Mechanical Engineering,

Indian Institute of Technology Madras, Chennai 600036, India

(Dated: August 20, 2019)

Abstract

It is known from recent studies that evaporation induces flow around a droplet at atmospheric conditions. This flow is visible even for slowly evaporating liquids like water. In the present study, we investigate the influence of the ambient gas on the evaporating droplet. We observe from the experiments that the rate of evaporation at atmospheric temperature and pressure decreases in a heavier ambient gas. The evaporation-induced flow in these gases for different liquids are measured using particle image velocimetry (PIV) and found to be very different from each other. However, the width of the disturbed zone around the droplet is seen to be independent of the evaporating liquid and the size of the needle (for the range of needle diameters studied), and only depends on the ambient gas used.

*Electronic address: anand@iitm.ac.in

†Electronic address: shamit@iitm.ac.in

I. INTRODUCTION

Evaporation of droplets is of great interest in many applications involving evaporating sprays, evaporative coolers, printing, coating, painting, etc. Thus, it has been studied extensively for a long time. The calculation of the rate of evaporation can be made using the classical model of Maxwell[1] which is based on a purely diffusion-driven process. This method has been extended and used to calculate the evaporation rates of sessile and pendant droplets by several investigators [2–4]. However, the evaporation process, even under atmospheric temperatures and pressures, is influenced by different effects; such as cooling effect [5–7], internal circulation [8–10], suspender or substrate effect [11, 12], and evaporation-induced flow effect [13–16]. Even in the case of a slow evaporating sessile droplet of water, the process of evaporation is influenced by the natural convection around the droplet [17]. The objective of the present work is to understand the influence of the difference in density between the surrounding gas and the vapor on the evaporation-induced flow and evaporation rate.

The difference in density is due to both thermal and solutal (molecular weight) effects. As evaporation cause cooling, the thermal effects cannot be eliminated or controlled easily in evaporation experiments. But, the solutal effect can be varied in degrees by changing the surrounding gas and the liquid (i.e., the difference in molecular weight between the gas and the vapor). This is the method adopted here, and we study the change in the resulting thermo-solutal flow and its effect on evaporation.

The natural convection induced by evaporation was studied by earlier researchers both experimentally [18, 19] and numerically [5, 20]. The possibility of this flow was indicated by Hegseth et al. [8]. In an earlier work, O'Brien and Saville [21] indicated the presence of vapor-phase convection around an evaporating sessile droplet using an interferometric technique. In more recent times, Dehaeck et al. [15] measured the vapor cloud around an evaporating droplet more precisely using digital holographic interferometry. Kelly-Zion et al. [13] used a schlieren imaging technique to demonstrate the presence of evaporation-induced buoyancy driven flow around a sessile droplet. The evaporation rate also increased in the presence of this flow.

Somasundaram et al. [18] quantitatively measured the evaporation-induced flow using the PIV technique for a very low Grashof number (of the order of one). They performed experi-

ments to show conclusively that the flow during the evaporation is largely due to the density difference, which in turn is due to the combined effect of temperature difference (thermal buoyancy) and molecular weight difference (solutal buoyancy). Although the difference in molecular weight between water and nitrogen suggests that the evaporation-induced flow should be upward for a water droplet evaporating in a nitrogen ambient, the observed flow is downward. These results show that thermal buoyancy is dominant in case of an evaporating water droplet in that configuration. However, it remains unknown as to how the flow may get modified when the solutal effects are varied by changing the ambient gas and the evaporating liquid.

One method to study the effect of solutal buoyancy alone in a situation similar to droplet evaporation is to study an equivalent process where a sessile droplet of one liquid slowly dissolves in an ambient of another. This can be seen in the experiments conducted by Dietrich et al. [19] where they visualized the induced flow in the dissolution process of a sessile drop of a small chain alcohol in water using the μPIV technique. They observed that the transition from diffusive to convective regime takes place for a solutal Rayleigh number of 12. However, in evaporation experiments, it is not easy to study the solutal effects alone, as the thermal effect is inevitably present. Very recently, Kelly-Zion et al. [22] proposed a correlation considering the diffusion and buoyancy effects for sessile droplet evaporation. Among other things, they report that the type of the ambient gas strongly influences the relative contribution of diffusion and convection in sessile droplet evaporation.

From these studies, it is understood that thermo-solutal buoyancy strongly influences the droplet evaporation process. However, the effect of it on the induced flow is still unclear. Here, we attempt to study the effect of thermo-solutal buoyancy on droplet evaporation by changing the ambient gas, primarily for two different evaporating liquids (non-volatile and volatile). The molecular weights of the ambient gases are selected in such a way that a wide range of density differences between the gas and vapor can be investigated. From the results, we show that the change in the molecular weight of the ambient gas changes the characteristics of the induced flow, and this influences the rate of evaporation. Ethanol and water are used as the evaporating liquids for most of the experiments. Droplets of these are suspended using a steel needle in a closed chamber under atmospheric pressure and temperature. The different ambient gases used are nitrogen (N_2), oxygen (O_2), argon (Ar), carbon dioxide (CO_2,) and sulfur hexafluoride (SF_6). The approximate differences in the density

(at atmospheric conditions) between water vapor and nitrogen, oxygen, argon, carbon dioxide, and SF_6, are -0.7, -0.9, -1.2, -1.4, and -5.5 kg/m^3 respectively. The density differences between ethanol vapor and the same gases as before are 0.8, 0.6, 0.3, 0.1, and 4.1 kg/m^3 respectively. Thus, a wide range of density differences between the vapor and the ambient gas is examined. The induced flow direction and characteristics change with this density difference. Thus, the flow around an evaporating droplet can be tailored by appropriately choosing an ambient gas. An ambient which effectively inhibits the surrounding flow may give an opportunity to study pure diffusion-driven evaporation.

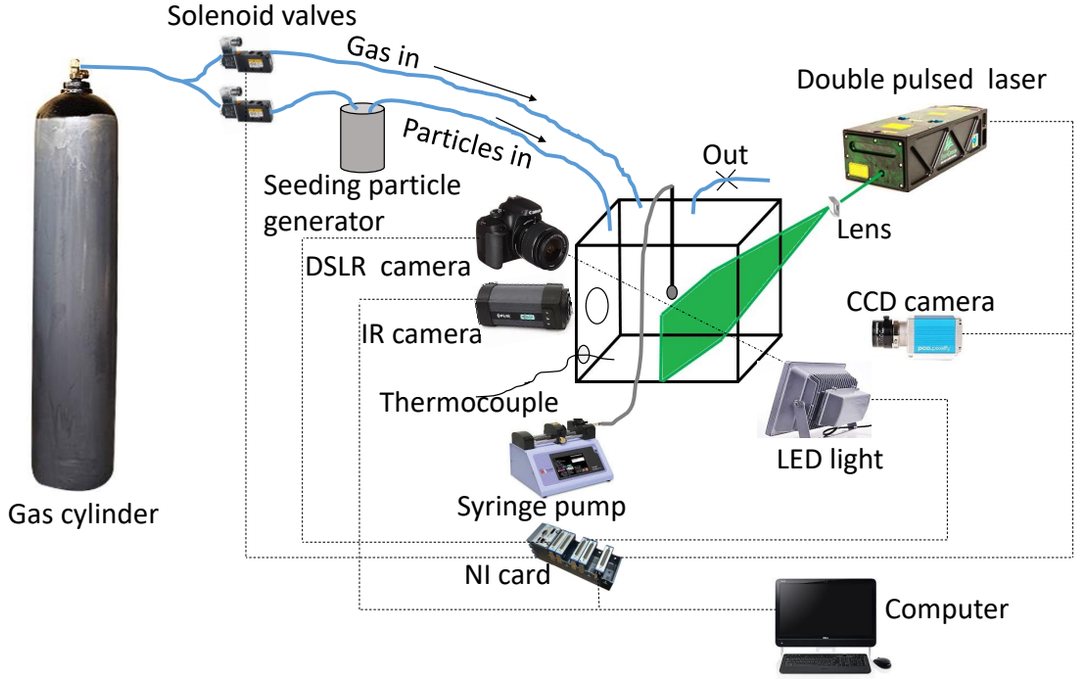

FIG. 1: Schematic diagram of the experimental setup.

II. EXPERIMENTAL SETUP AND METHOD

A schematic of the experimental setup is shown in Fig. 1. A cubical glass chamber fixed on a metal frame (24 cm in each side) is used for the pendant droplet evaporation studies. The top plate of the chamber has separate vent holes connected to hoses through solenoid controlled valves. They are used to introduce the required ambient gas and the seeding particles into the chamber. One of the vent holes is open to the atmosphere. As indicated before, an ethanol or water droplet is used as the evaporating liquid in different

ambient gases (N_2, O_2, Ar, CO_2, and SF_6 gas). Sesame oil droplets are used as seeding particles for the particle image velocimetry (PIV) studies [23]. The chamber is maintained at atmospheric pressure and room temperature. The room temperature is maintained at 28 $\pm 1^{\circ}$C. The temperature of the chamber is measured with a K-type thermocouple fitted into the chamber. It is inserted inside the test rig through a hole made at the corner of one of the glass walls. A steel needle (inner diameter = 2.6 mm, thickness = 0.5 mm) is inserted from the top plate to suspend the required amount of liquid. A known volume of liquid is injected from a 25 mL Hamilton syringe by operating a syringe pump which can inject at a minimum flow rate of 1.28 pL/min. A LED (light-emitting diode) backlight and a Nikon DSLR (digital single-lens reflex) camera of resolution 2400 X 1600 pixels fitted with a 105 mm macro lens are used to capture images of the evaporating droplet at regular intervals. The induced flow around the evaporating droplet is visualized using the particle image velocimetry (PIV) technique. A laser sheet is formed to illuminate the seeding particles using a double-pulsed laser and a 20 mm focal length plano-convex lens. A double shutter CCD (charge-coupled device) camera of resolution 1392 X 1040 pixels fitted with a 50 mm lens is used to capture the flow of the seeding particles. These two measurements (backlight imaging and PIV) are performed simultaneously with the help of a National Instruments card connected to a computer. Droplet surface temperature is measured using an infra-red (IR) thermal imaging camera (FLIR T250) of resolution of 320 x 240 pixels. Since the glass sides of the setup are opaque to IR light, a hole is made in one wall for the IR camera to image through, which is kept covered with a plastic sheet at other times. It is confirmed that the evaporation rate of the droplet does not change when this window is open or sealed.

Initially, the chamber is purged with the selected ambient gas (99.99% pure). The same gas with seeding particles (sesame oil, d $\approx$ 2 μm) is introduced using the solenoid valve controller. It may be noted that the Stokes number for such small particles is very small and hence they faithfully follow the air flow for all the ambient gases used. The time to pass the gas and seeding particles is chosen as mentioned in Somasundaram et al. [18] to ensure that the evaporation rate is not influenced by the seeding density. The settling velocity of the sesame oil particles used for PIV was measured in the absence of the evaporating droplet. The magnitude of velocity was 0.09$\pm$0.02 cm/s in the nitrogen ambient and 0.008$\pm$0.002 cm/s in the SF_6 ambient. The smallest velocities in the field may be comparable with the settling velocities. However, the objective of this paper is not to capture accurately the

smallest velocities in the field of view, but, to study the dependence of the evaporation-induced velocities on the choice of the ambient gas. The measurements presented here are sufficiently accurate for this purpose, even with the slow settling of the seeding particles.

A volume of approximately 20 μL of the test liquid (99.9% pure ethanol or HPLC (high pressure liquid chromatography) grade water) is used for experiments. The droplet is allowed to evaporate in the presence of the selected ambient gas. Shadow images of the evaporating droplet are acquired at 5 s intervals using the Nikon DSLR camera and LED light. These images are processed with the help of a MATLAB code to determine the volume-equivalent (spherical) diameter of the droplet as a function of time. PIV images are acquired using the laser sheet and the double shutter camera. These images are processed with the open source 'PIVlab'[24] software to obtain the velocities of induced flow. In the post-processing of the PIV measurements, the region of interest (ROI) is divided into small interrogation windows. Multi-pass processing is used to obtain the velocity vectors in the interrogation windows. The minimum size of the interrogation window used is 16×16 pixels. For sub-pixel accuracy, the Gaussian fit is used for vector interpolation, leading to a spatial accuracy of less than a pixel. In this way, the images are processed to obtain velocity vectors. For the recording parameters used in the present experiments, the accuracy varies between 0.01-0.04 cm/s. The correlation coefficients of the processed images are ensured to be always greater than 0.75. A minimum of 5 experiments are performed for each condition.

III. RESULTS AND DISCUSSION

A. Evaporation rate comparison

The variation of the normalized square of the diameter $\left(\frac{d^2}{{d_0}^2}\right)$ with time $\left(\frac{t}{{d_0}^2}\right)$ is compared for different ambient gases in Fig. 2. The slope of this line is the evaporation constant. The evaporation constants of ethanol and water droplets evaporating in different ambient gases are compared in Table I. It can be seen from this table that denser gases (with higher molecular weights) inhibit the evaporation of both ethanol and water. In SF_6, the evaporation rate of ethanol is 37% less than that in nitrogen. For water, this reduction is close to 70%. Thus, it is clear from the results that the ambient gas has a strong influence on the evaporation rates of both slow and rapidly evaporating droplets at atmospheric conditions.

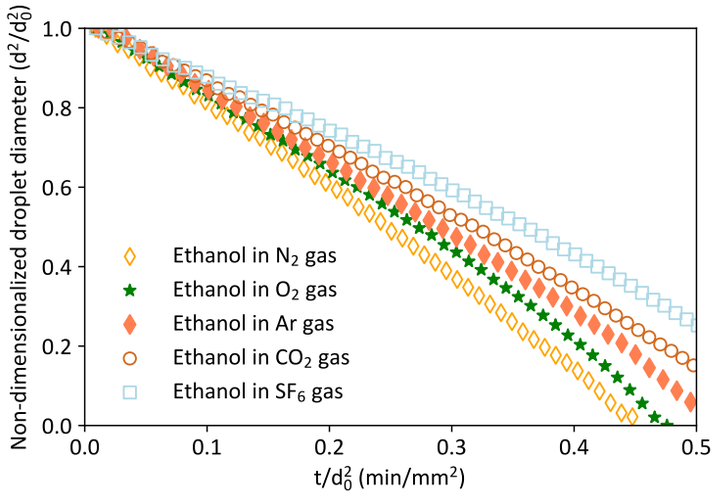

(a)

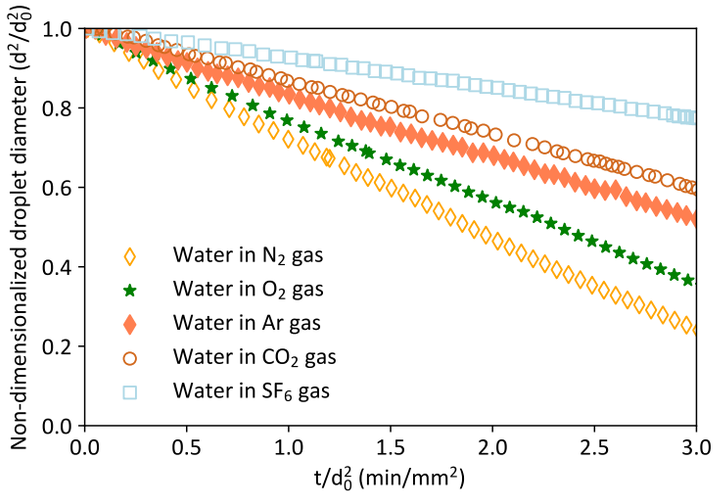

(b)

FIG. 2: Variation of the square of non-dimensionalized droplet diameter with time for evaporating droplets of a) ethanol and b) water in different ambient gases (d_0 is the initial droplet diameter).

The surface temperature of the evaporating droplets is measured during droplet evaporation using the thermal imaging camera. The uncertainty in the measured absolute temperature is $\pm$ 2°C . The variation in the minimum measured temperature on the surface of the droplet with time is shown in Fig. 3 for ethanol and water droplets.

As seen in Fig. 3, the droplet surface cools below the ambient during evaporation. The

TABLE I: Comparison of the evaporation constant of ethanol and water droplets evaporating in the different ambient gases.

		Evaporation constant
Liquid	Ambient gas	mm^2/min
Ethanol	N_2	2.25±0.08
	O_2	2.1±0.04
	Ar	1.9±0.03
	CO_2	1.7 ±0.06
	SF_6	1.3±0.045
Water	N_2	0.23 ± 0.02
	O_2	0.2± 0.01
	Ar	0.17 ±0.01
	CO_2	0.15±0.013
	SF_6	0.07±0.007

cooling, as expected, is more in nitrogen ambient due to higher evaporation rates. In SF_6, the cooling is less. The cool vapor from the droplet surface descends, creating a flow around the droplet. This is shown clearly in Fig. 4 where we present the measured steady velocity field from PIV for a quasi-steady convective plume. The quasi-steady state is ascertained based on the measured maximum flow velocity. After this quasi-steady state is attained, the variation in maximum flow velocity is very little. It can be seen from Fig. 4a that the descending ethanol vapor entrains more ambient nitrogen and oxygen than argon or carbon dioxide. For SF_6, the induced flow is much less and is directed upwards, indicating the dominance of the solutal buoyancy effect. In contrast, for a water droplet (Fig. 4b), the flow is directed downwards for all the ambient gases, showing the dominance of the thermal buoyancy effect. As with ethanol, for water, we see that the flow entrained is more for nitrogen and slowly goes down as we move towards heavier gases. The stronger entrained flow disperses and rapidly distributes the vapor in the surroundings, and thus enables faster evaporation.

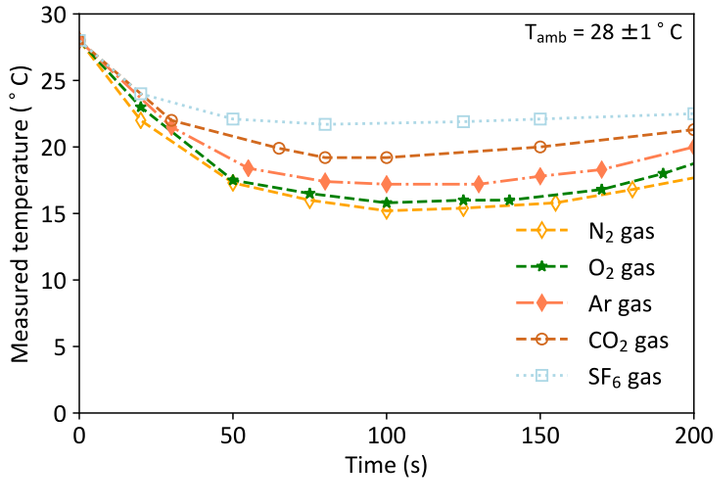

(a)

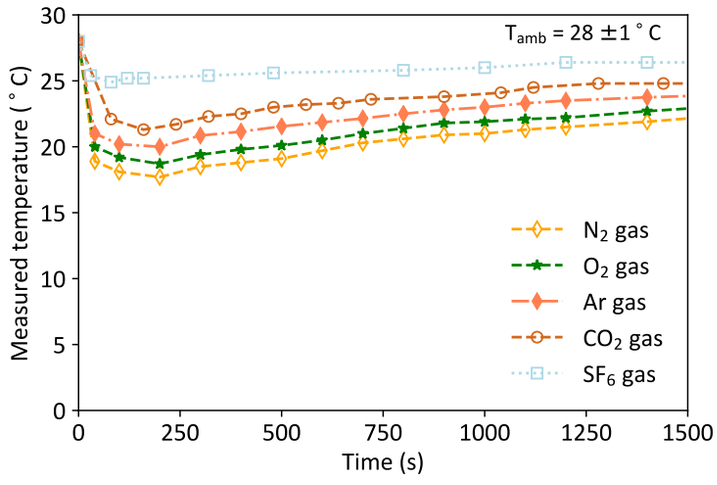

(b)

FIG. 3: Comparison of the measured surface temperature of a) ethanol and b) water droplets evaporating in the different ambient gases with time.

B. Velocity profile below the droplet in different gases

In the previous section, we presented the overall structure of the convective plume induced by a droplet evaporating in different gases. Here, we look at the velocity profile of this induced flow below the droplet. The velocity reported here is measured when the plume attains a quasi-steady state, at 50 s and 200 s after the start of evaporation, for ethanol and water droplets respectively. Again, there is a developed region in the flow and we look at the

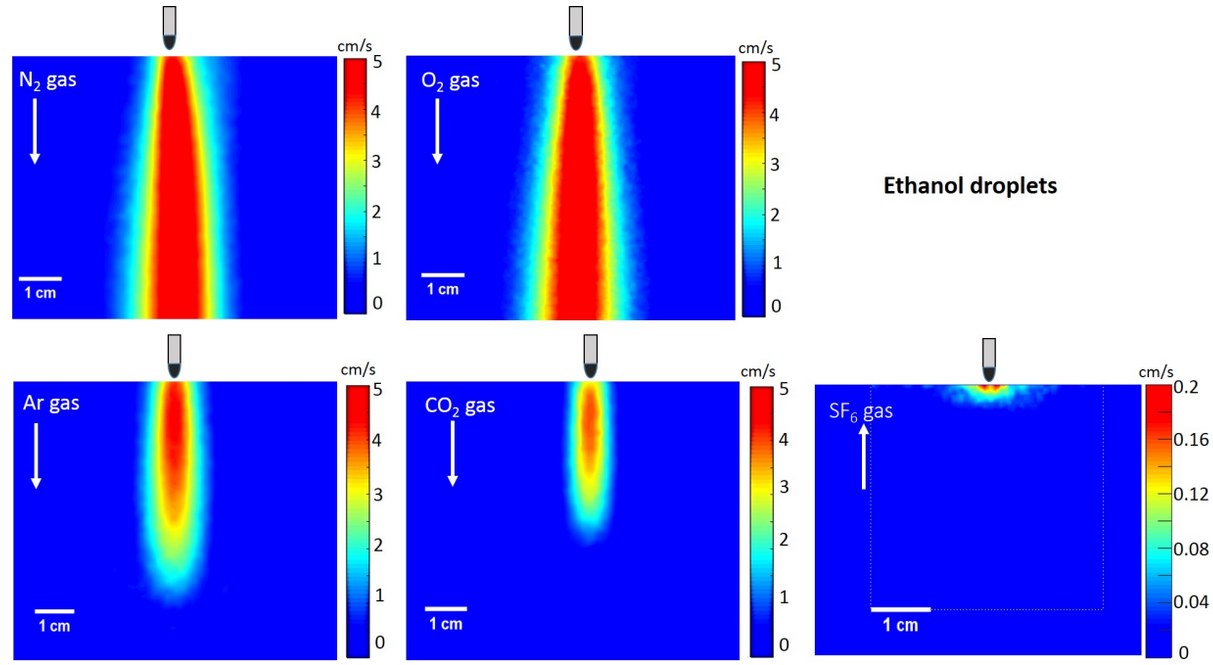

(a)

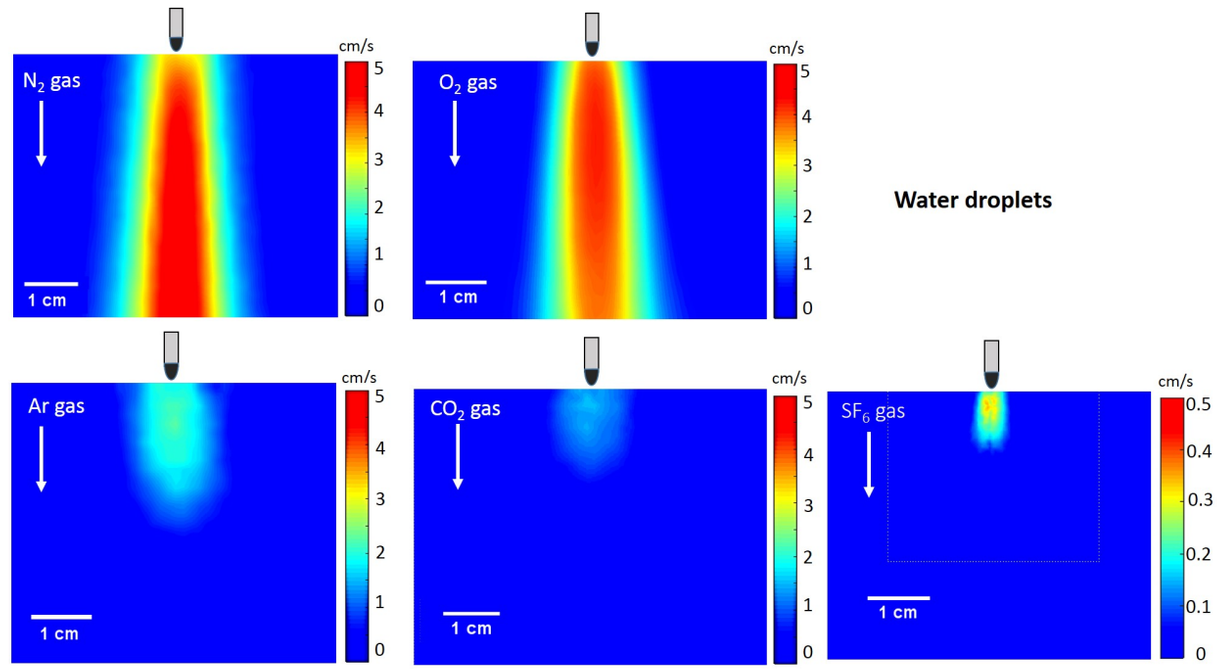

(b)

FIG. 4: Comparison of the velocity magnitudes of the flow induced around an evaporating (a) ethanol (multimedia view) and (b) water (multimedia view) droplet, in different ambient gases. The arrow indicates the direction of the flow. The suspended droplet shown in each case is merely a representation, and is not to scale. Note: The colorbar is different for SF_6.

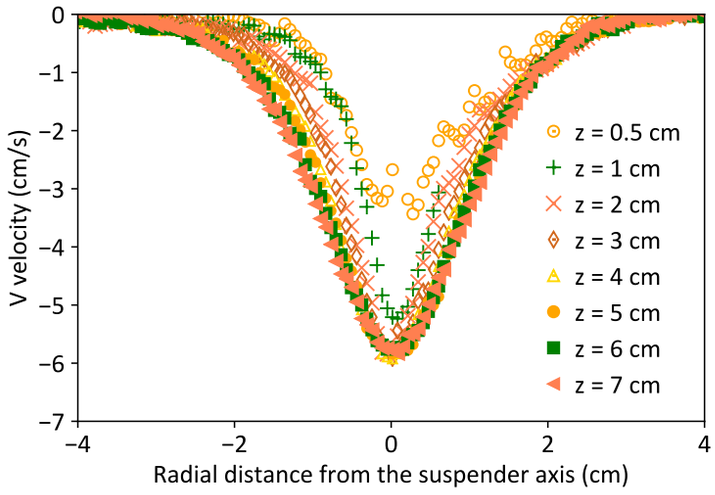

FIG. 5: Comparison of V velocity (vertical component) profiles plotted at different vertical locations (z) below the tip of the suspender (for ethanol evaporating in nitrogen gas). z = 0 represents the tip of the suspender.

velocity profile in this region. In Fig. 5 the velocity profiles are given at different locations below the tip of the suspender (z = 0) for an ethanol droplet evaporating in nitrogen. In this figure, the developed flow is attained at approximately 4 cm below the suspender, after which the velocity profile remains unchanged. The location of this region varies depending on the ambient gas. Figure 6 shows the induced flow profiles below ethanol (left) and water (right) droplets. The velocity reported in Fig. 6a is measured at a distance of 6 cm below the tip of the needle for ethanol/water evaporating in nitrogen and oxygen. For an ethanol droplet in argon and carbon dioxide, the velocity profiles at a location of 2 cm and 1.2 cm below the tip of the needle respectively, are plotted. For SF_6, the flow subsides at approximately 0.6 cm below the needle tip; hence, the velocity profile is reported at 0.4 cm below the needle tip. Similarly, for a water droplet, the velocity profiles at 1.5 cm, 0.8 cm and 0.6 cm below the tip of the needle in argon, carbon dioxide and SF_6 respectively, are plotted. In Fig. 6b, the non-dimensional velocity (velocity is non-dimensionalized with the maximum centerline velocity, V_{max}) is plotted against the radial distance from the axis of the suspender for ethanol (left) and water (right) droplets. Accuracy and precision of the centerline velocity are ascertained. Considering the accuracy and precision to be independent and propagating them using the quadrature law gives a total uncertainty of 2.3% for ethanol in nitrogen and 12.9% for ethanol in SF_6 which is the highest value of all the cases. Maximum flow velocities

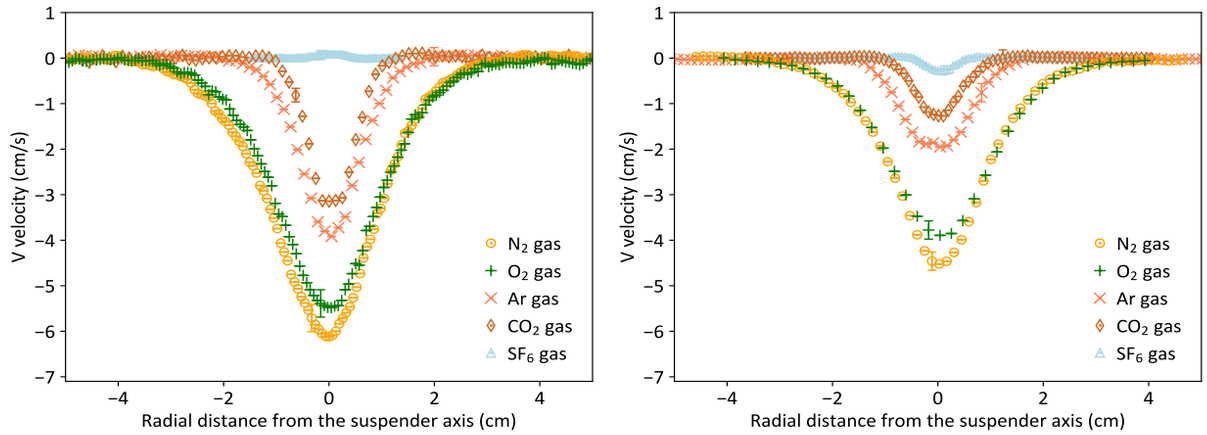

(a)

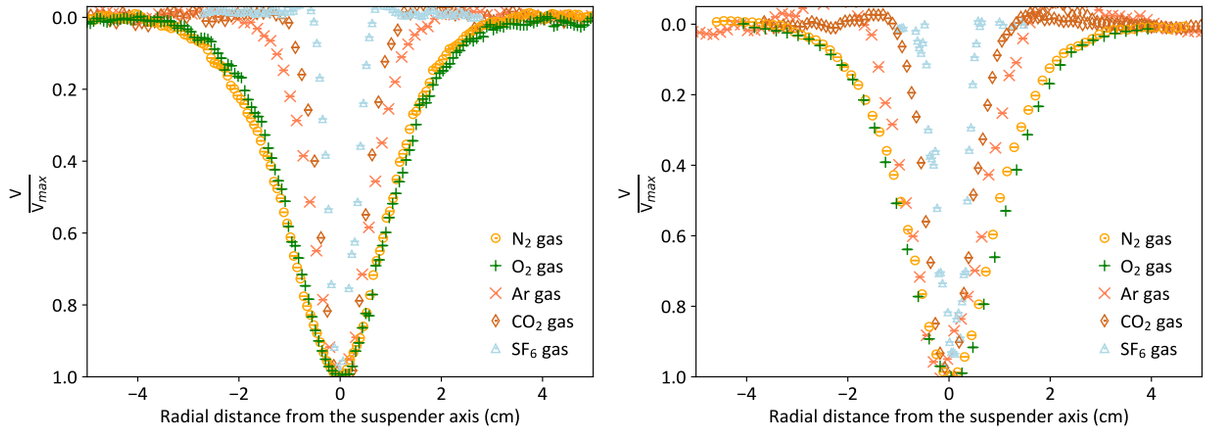

(b)

FIG. 6: a) Comparison of velocity (vertical component) variation with distance from the axis of the suspender for evaporating ethanol (left) and water (right) droplets in different ambient gases. b) Data as in (a) above, non-dimensionalized with V_{max}. For the ethanol droplet evaporating in SF_6, the curve has been inverted.

of nearly 6 cm/s and 5.7 cm/s are observed for an ethanol droplet evaporating in nitrogen and oxygen respectively. When the ambient gas is changed to argon, the maximum flow velocity is reduced to approximately 4 cm/s. It is further reduced to 3.5 cm/s in carbon dioxide. However, in the case of SF_6, the induced flow is upwards with a maximum velocity of 0.1 cm/s below the droplet. This can be seen in Fig. 6a. In the case of the water droplet, the maximum velocities below it are 4.3 cm/s, 4 cm/s, 2 cm/s, 1.1 cm/s and 0.2 cm/s for nitrogen, oxygen, argon, carbon dioxide, and SF_6 respectively. So, we can observe from

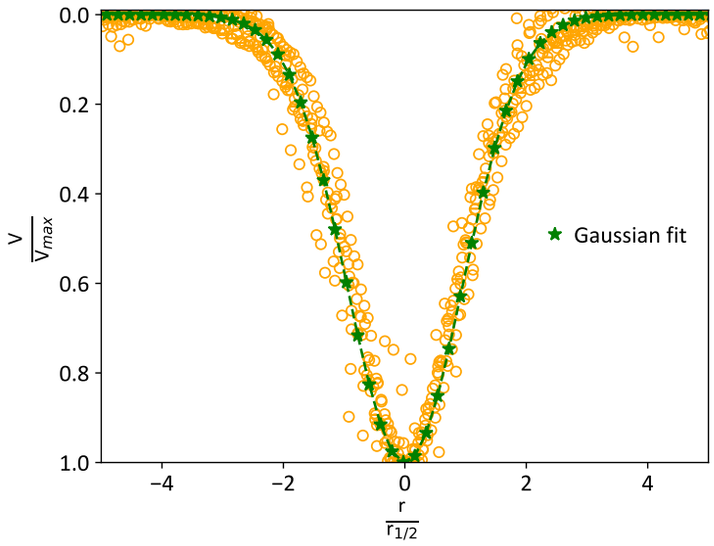

FIG. 7: Self similarity in the flow due to the evaporating ethanol and water droplets in different ambient gases ($r_{1/2}$ is the radial distance at which the velocity becomes half of V_{max}).

Fig. 6 that the induced flow is strongest in nitrogen and weakest in SF_6. The width of the disturbed region around the droplet is maximum for nitrogen and least for SF_6. Interestingly, the induced flows around the evaporating ethanol and water droplets in different gases are all self-similar in nature as shown in Fig. 7. As the present case resembles a steady plume originating from a point source, a Gaussian fit represents the velocity profile well [25–27]. The general convective plume structure can be defined for the self-similar curves using the Gaussian distribution,

$$\frac{v}{v_{max}} = 0.97 * exp - (\frac{\frac{r}{r_{1/2}} + 0.001}{1.343})^2. \quad (1)$$

The penetration length of the plume also varies with respect to the ambient gases, as seen from Table II. The penetration length of the vapor mixture is defined here as the distance from the tip of the needle to the point along the needle axis at which the vertical velocity is close to zero. The flow penetration lengths of the evaporating ethanol/water droplets were more than 7 cm in nitrogen and oxygen beyond which they could not be measured due to a limitation of the laser-illuminated area. The penetration length is 6±0.2 cm and 4.8±0.1 cm for an ethanol droplet evaporating in argon and carbon dioxide respectively. For a water droplet, it is 3±0.1 cm and 2±0.2 cm respectively in argon and carbon dioxide.

TABLE II: Comparison of the flow penetration lengths due to ethanol and water droplets evaporating in the different ambient gases.

Liquid	Ambient gas	Penetration length (cm)
Ethanol	N_2	> 7
	O_2	> 7
	Ar	6±0.2
	CO_2	4.8±0.1
	SF_6	Flow is upwards
Water	N_2	> 7
	O_2	> 7
	Ar	3±0.1
	CO_2	2±0.2
	SF_6	1±0.2

The penetration length is the least for the droplets evaporating in SF_6. It is approximately 1±0.2 cm for a water droplet and is not detectable for the ethanol droplet due to the upward flow. The penetration length mostly depends on the difference in densities between the gas-vapor mixture at the droplet surface and the ambient gas ($\Delta\rho$). A simple calculation of the density difference ($\Delta\rho$) is made, using the ideal gas equation of state and simple mixing laws, assuming that the interface is at equilibrium. The mixture temperature is taken as the measured droplet surface temperature, and the gas is taken to be at the ambient temperature. For ethanol vapor in different gases, the value of $\Delta\rho$ in kg/m^3 comes out to be 0.078 (nitrogen), 0.076 (oxygen), 0.06 (argon), 0.05 (carbon dioxide), and -0.18 (SF_6). It can be seen that the decreasing trend in $\Delta\rho$ correctly predicts the lower velocity magnitudes and penetration lengths of the evaporation-induced flows observed in these different gases. So, the differences in penetrations in different gases are due to the different values of relative densities between the gas-vapor mixture and the gas. Next we look at the width of the disturbed zone.

The width of the disturbed zone in the gas phase is defined as the maximum width of the

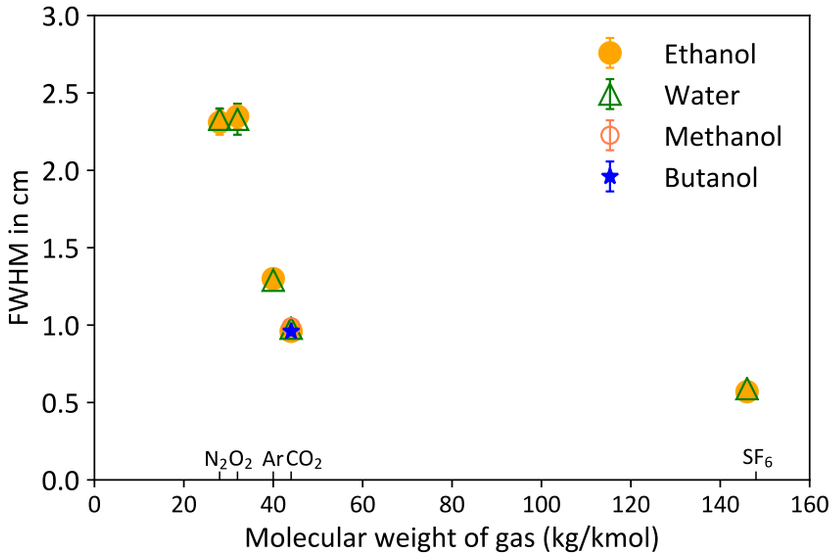

FIG. 8: Comparison of the full width at half maximum (FWHM) for all the evaporating droplets used in different ambient gases. The error bars indicate the standard deviation of the measured values.

gas which is disturbed in the developed flow. It can be noted from Fig. 6 that the width of the disturbed zone in the ambient is strongly dependent on the ambient gas. The values of the width are found to be 7.1±0.3 cm, 6.9±0.2 cm, 4±0.1 cm, 2.4±0.1 cm, and 1±0.1 cm in nitrogen, oxygen, argon, carbon dioxide and SF_6 respectively. The variation of the full width at half maximum (FWHM) with the molecular weight of ambient gas is shown in Fig. 8. The FWHM is defined for all the cases based on the Gaussian fit which was a good approximation for the present work. The FWHM is seen to be identical for the droplets of different liquids evaporating in the same ambient gas. It is also evident from Fig. 8, that the width of the disturbed zone is dependent on ambient gas. In our understanding, the edge of the plume is mostly constituted of the ambient gas while the core has a mixture of the vapor and the ambient gas. So, the width of the entrained region depends largely on the ambient gas. This hypothesis can be confirmed by making measurements of the vapor mass fraction in the plume. Such measurements are, however, not easy in the present situation, as both the temperature and mass fraction vary in the plume. Most measurement techniques such as schlieren cannot make distinctions between the density variations due to changes in temperature and those due to varying mass fractions.

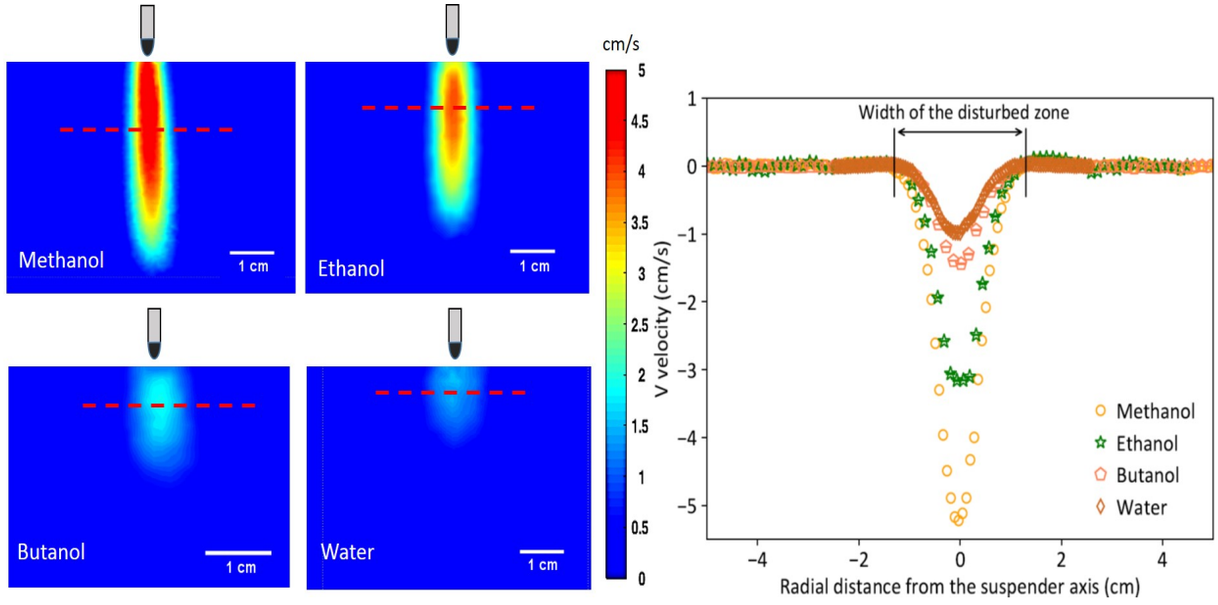

FIG. 9: Velocity contours due to different liquids evaporating in CO_2 gas are shown in the figure on the left. The suspended droplet shown in each case is just a representation and is not to scale. The figure on the right shows a comparison of the velocity (vertical) profiles corresponding to the location marked by the dashed red line (in the fully developed region) in the figure on the left.

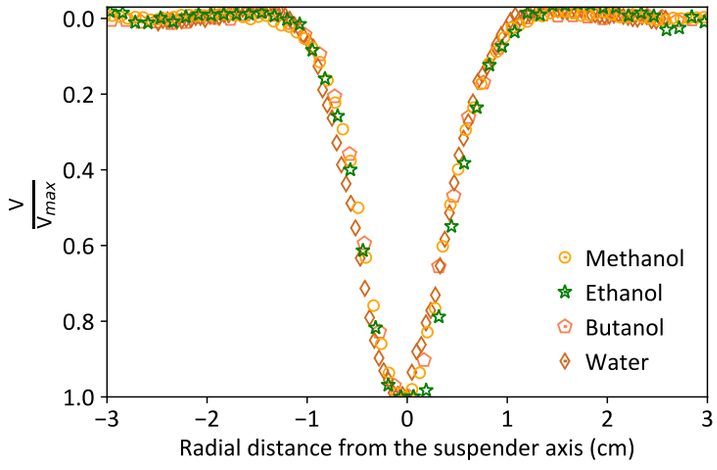

FIG. 10: Comparison of the velocity (scaled with V_{max}) profiles due to different liquids evaporating in CO_2 ambient gas.

C. Evaporation-induced flow for different liquids

In the previous section, we saw that both the penetration and the width of the evaporation-induced plume is dependent on the ambient gas. In this section, we try to ascertain the effect of the evaporating liquid on the flow induced in the ambient. Figure 9 shows the flow induced by methanol, ethanol, butanol, and water droplets in carbon dioxide ambient. The left side of this figure shows plots of the velocity magnitude. On the right side of this figure, the velocity profiles at 2.5 cm, 1.2 cm, 1 cm and 0.8 cm below the needle tip for methanol, ethanol, butanol and water respectively, are plotted. The penetration of the plume depends on the volatility of the evaporating liquid. Methanol penetrates the most, and water the least. However, as seen in the right side of Fig. 9, the width of the disturbed zone is independent of the evaporating liquid. Fig. 10 also clearly shows that the velocity profiles collapse onto each other when the velocity is non-dimensionalized and the distance is retained dimensional. Similar results are also observed when experiments are done with nitrogen as the ambient gas. Insights into this are sought in the following section.

D. Evaporation-induced flow for different suspenders

From the previous sections, we see that the maximum velocity and penetration length of induced flow changes with either ambient gas or evaporating liquid. However, the width of the disturbed zone is not dependent on the liquid. In this section, we examine the effect of the size of the suspender. The needle diameters considered are as shown in Fig. 11. The length of the needles is kept constant as 12 cm. The outer diameters (D_0) of the needles are 2.7 mm, 2.1 mm, and 1 mm. Ethanol is used as the evaporating liquid in nitrogen or carbon dioxide ambient. The evaporation constants and induced flows below the droplet are shown in Fig. 12 and Fig. 13 respectively. The evaporation constants and the induced flows are similar for the 2.7 mm and 2.1 mm needles. The 1.07 mm needle shows a slower evaporation rate and less pronounced induced flow. The reasons for this reduced evaporation rate have been discussed elsewhere (Radhakrishnan et al. [11]). Although there is a change in the convective plume structure between the needle diameters of 2.7 mm and 1 mm, the width of the disturbed zone in the developed flow is not changed, as shown in Fig. 14. Hence, the width of the disturbed zone is independent of the evaporating liquid and needle diameter

and only depends on the ambient gas used, for the needle diameters studied. So, again we see that the penetration reduces with reducing needle and droplet size but the FWHM of the disturbed zone is independent of needle and droplet size. This is a further evidence that the edge of the plume is mostly constituted of the ambient gas with the core being a mixture of the vapor and the ambient gas. So, the width of the entrained region is largely dependent on the ambient gas and not the needle or droplet size. In the present experiments, the droplet and needle sizes are much less than the width of the disturbed zone. As they become comparable, the width of the disturbed zone is expected to increase.

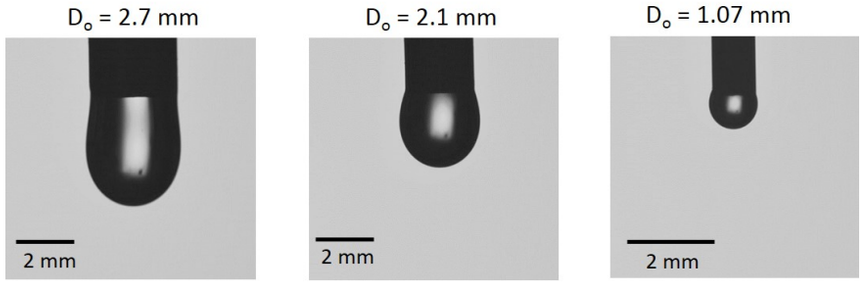

FIG. 11: Representative images of ethanol droplets evaporating from the needles of different diameters (D_0).

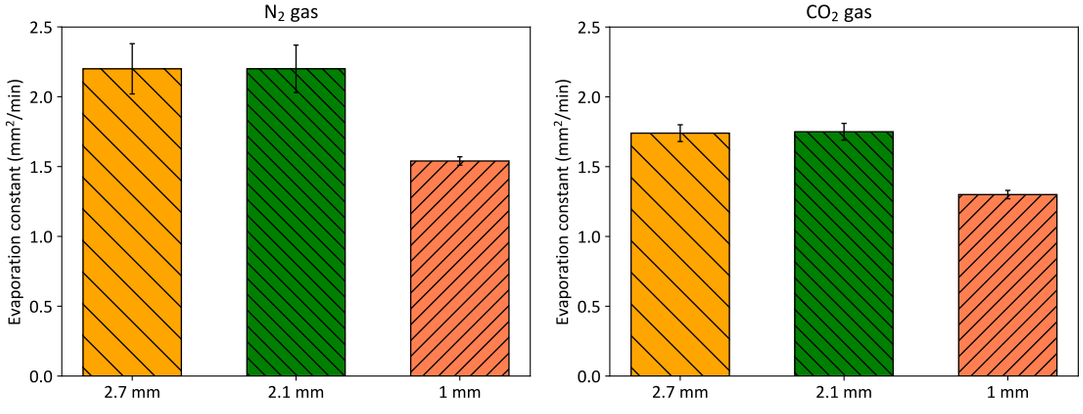

FIG. 12: Comparison of the evaporation constants of ethanol droplets suspended from needles of different diameters in N_2 and CO_2 ambient gases. The error bars indicate the standard deviation of the measured value.

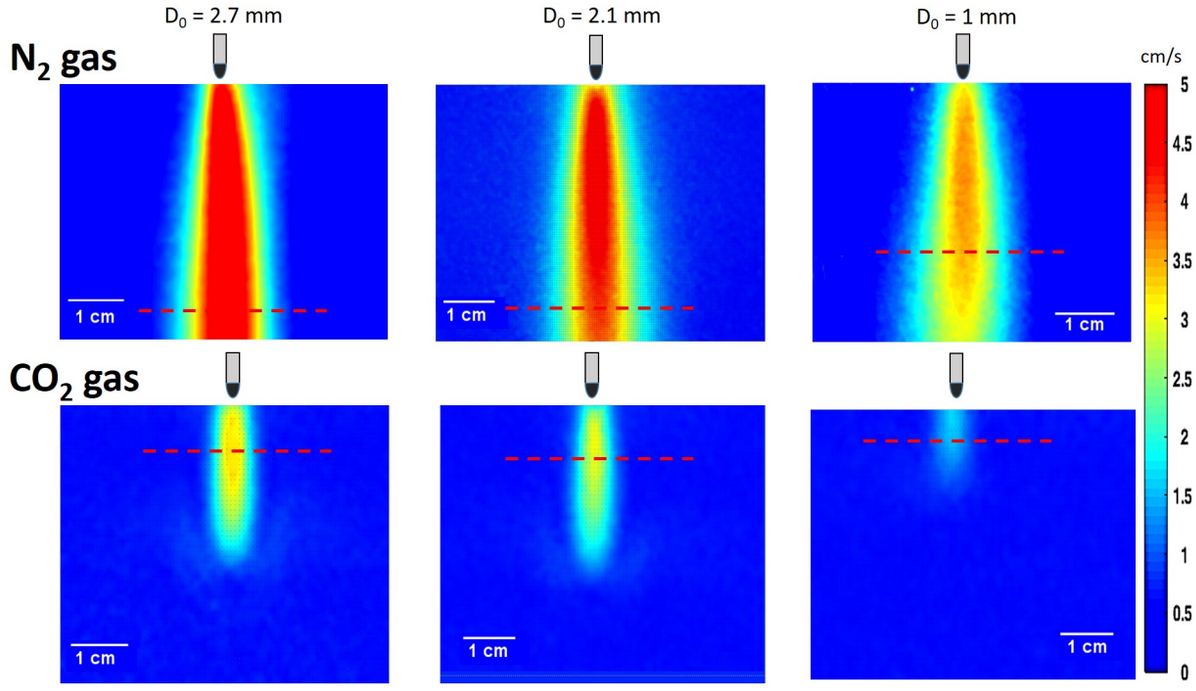

FIG. 13: Velocity contours of the flow below an ethanol droplet evaporating from needles of different diameters in N_2 and CO_2 ambient gas. The suspended droplet shown in each case is merely a representation and is not to scale.

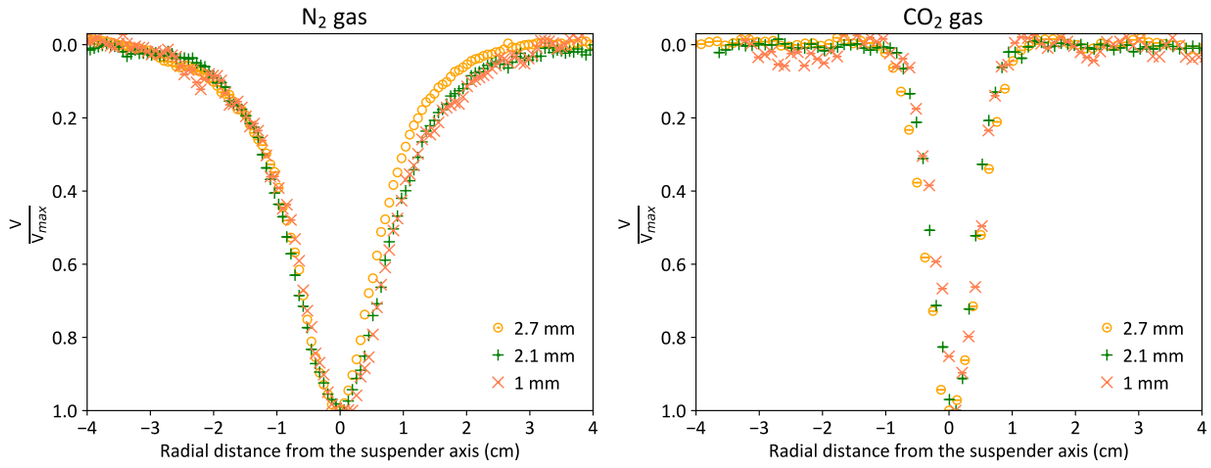

FIG. 14: Comparison of the velocity (non-dimensionalized with V_{max}) profiles in N_2 and CO_2 ambient gas induced by ethanol droplets evaporating from needles of different diameters.

IV. CONCLUSION

In this work, the natural convection outside the droplet was studied experimentally with ethanol and water droplets evaporating in different ambient gases. It was observed that the rate of evaporation of an ethanol/water droplet decreases in a heavier ambient gas. Thus, the evaporation-induced flow around the droplet is dependent on the ambient gas. In nitrogen, the evaporation rate and the induced flow are more, whereas, those in the case of an SF_6 ambient are less. The velocity profile was measured, and it was shown to demonstrate self-similarity. The penetration of the induced flow is more for a higher evaporation rate and in a lighter ambient medium. However, the width of the disturbed region in the induced flow around the droplet is independent of the evaporating liquid and the suspender size and only depends on the ambient gas used.

[1] W. Niven, *The Scientific Papers of James Maxwell* (Dover Publications, Inc., 1965).

[2] R. G. Picknett and R. Bexon, Journal of Colloid And Interface Science **61**, 336 (1977), ISSN 00219797.

[3] H. Hu and R. G. Larson, Journal of Physical Chemistry B **106**, 1334 (2002), ISSN 10895647.

[4] Y. O. Popov, Physical Review E - Statistical, Nonlinear, and Soft Matter Physics **71**, 1 (2005), ISSN 15393755, 0408106.

[5] Z. Pan, J. A. Weibel, and S. V. Garimella, Langmuir **30**, 9726 (2014), ISSN 1520-5827, URL http://www.ncbi.nlm.nih.gov/pubmed/25105726{%}5Cnhttp://pubs.acs.org/doi/abs/10.1021/la501931x.

[6] X. Xu and L. Ma, Scientific Reports **5**, 38 (2015), ISSN 20452322.

[7] Y. Wang, L. Ma, X. Xu, and J. Luo, Journal of Colloid and Interface Science **484**, 291 (2016), ISSN 10957103, URL http://dx.doi.org/10.1016/j.jcis.2016.09.011.

[8] J. Hegseth, N. Rashidnia, and A. Chai, Physical Review E **54**, 1640 (1996), ISSN 1063-651X.

[9] R. Savino and S. Fico, Physics of Fluids **16**, 3738 (2004), ISSN 10706631.

[10] D. K. Mandal and S. Bakshi, International Journal of Multiphase Flow **42**, 42 (2012), ISSN 03019322.

[11] S. Radhakrishnan, N. Srivathsan, T. N. C. Anand, and S. Bakshi, International Journal of Thermal Sciences **140**, 368 (2019).

[12] G. J. Dunn, S. K. Wilson, B. R. Duffy, S. David, and K. Sefiane, Journal of Fluid Mechanics **623**, 329 (2009), ISSN 00221120.

[13] P. L. Kelly-Zion, C. J. Pursell, R. S. Booth, and A. N. VanTilburg, International Journal of Heat and Mass Transfer **52**, 3305 (2009), ISSN 00179310, URL http://dx.doi.org/10.1016/j.ijheatmasstransfer.2009.01.015.

[14] F. Carle, B. Sobac, and D. Brutin, Applied Physics Letters **102** (2013), ISSN 00036951.

[15] S. Dehaeck, A. Rednikov, and P. Colinet, Langmuir **30**, 2002 (2014), ISSN 1520-5827, URL http://www.ncbi.nlm.nih.gov/pubmed/24506092.

[16] B. Dollet and F. Boulogne, Physical Review Fluids **2** (2017), ISSN 2469990X, 1704.03243.

[17] O. Carrier, N. Shahidzadeh-Bonn, R. Zargar, M. Aytouna, M. Habibi, J. Eggers, and D. Bonn, Journal of Fluid Mechanics **798**, 774 (2016), ISSN 14697645.

[18] S. Somasundaram, T. N. C. Anand, and S. Bakshi, Physics of Fluids **27** (2015), ISSN 10897666.

[19] E. Dietrich, S. Wildeman, C. W. Visser, K. Hofhuis, E. S. Kooij, H. J. W. Zandvliet, and D. Lohse, Journal of Fluid Mechanics **794**, 45 (2016), ISSN 0022-1120, 1601.05226, URL http://www.journals.cambridge.org/abstract{_}S0022112016001580.

[20] M. Ait Saada, S. Chikh, and L. Tadrist, Physics of Fluids **22** (2010), ISSN 10706631.

[21] R. N. O'Brien and P. Saville, Langmuir **3**, 41 (1987).

[22] P. L. Kelly-Zion, C. J. Pursell, G. N. Wassom, B. V. Mandelkorn, and C. Nkinthorn, International Journal of Heat and Mass Transfer **118**, 355 (2018), ISSN 00179310, URL https://doi.org/10.1016/j.ijheatmasstransfer.2017.10.129.

[23] M. C. Jermy, Experiments in Fluids **33**, 321 (2002), ISSN 07234864.

[24] W. Thielicke and E. J. Stamhuis, *PIVlab-Time-Resolved Digital Particle Image Velocimetry Tool for MATLAB* (2014), URL http://dx.doi.org/10.6084/m9.figshare.1092508.

[25] K. Cederwall and J. D. Ditmars, *Proceedings of the 14th International Conference on Coastal Engineering* (1970).

[26] S. Yin, Y. Li, Y. Fan, and M. Sandberg, Building and Environment **149**, 79 (2019), ISSN 03601323, URL https://doi.org/10.1016/j.buildenv.2018.11.039.

[27] Z. Liu, P. Cooper, and P. W. Wypych, Journal of Particulate Science and Technology **25**, 357 (2007).

[28] K. Sefiane, S. K. Wilson, S. David, G. J. Dunn, and B. R. Duffy, Physics of Fluids **21** (2009), ISSN 10706631.

[29] H. V. Tran, T. A. Nguyen, S. R. Biggs, and A. V. Nguyen, Chemical Engineering Science **177**, 417 (2018), ISSN 00092509, URL https://doi.org/10.1016/j.ces.2017.12.003.

[30] F. Carle, S. Semenov, M. Medale, and D. Brutin, International Journal of Thermal Sciences **101**, 35 (2016), ISSN 12900729, URL http://dx.doi.org/10.1016/j.ijthermalsci.2015.10.012.

[31] R. D. Trengove and W. A. Wakeham, Journal of Physical and Chemical Reference Data **16**, 175 (1987), ISSN 15297845.

[32] F. J. Uribe, E. A. Mason, and J. Kestin, Journal of Physical and Chemical Reference Data **19**, 1123 (1990).

[33] R. C. Reid, J. M. Prausnitz, and B. E. Poling, *The Properties of Gases and Liquids* (McGraw-Hill, New York, 1987).

[34] P. Linstrom and W. Mallard, *NIST Chemistry WebBook* (NIST Standard Reference Database No. 69, National Institute of Standards and Technology, Gaithersburg, MD, 2014).

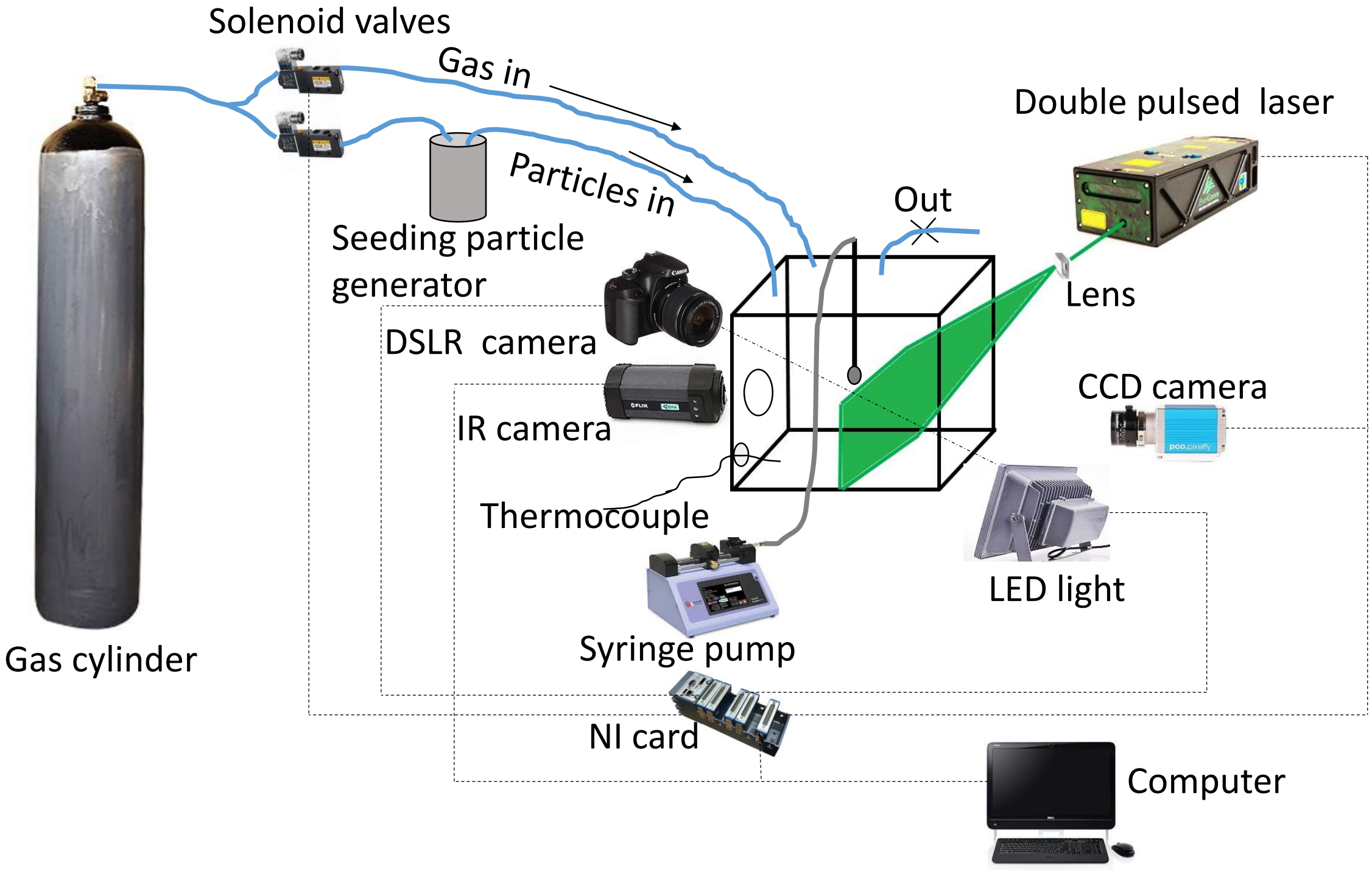
Solenoid valves
Gas in
Particles in
Seeding particle generator
Out
Double pulsed laser
Lens
DSLR camera
IR camera
CCD camera
Thermocouple
LED light
Syringe pump
NI card
Computer
Gas cylinder

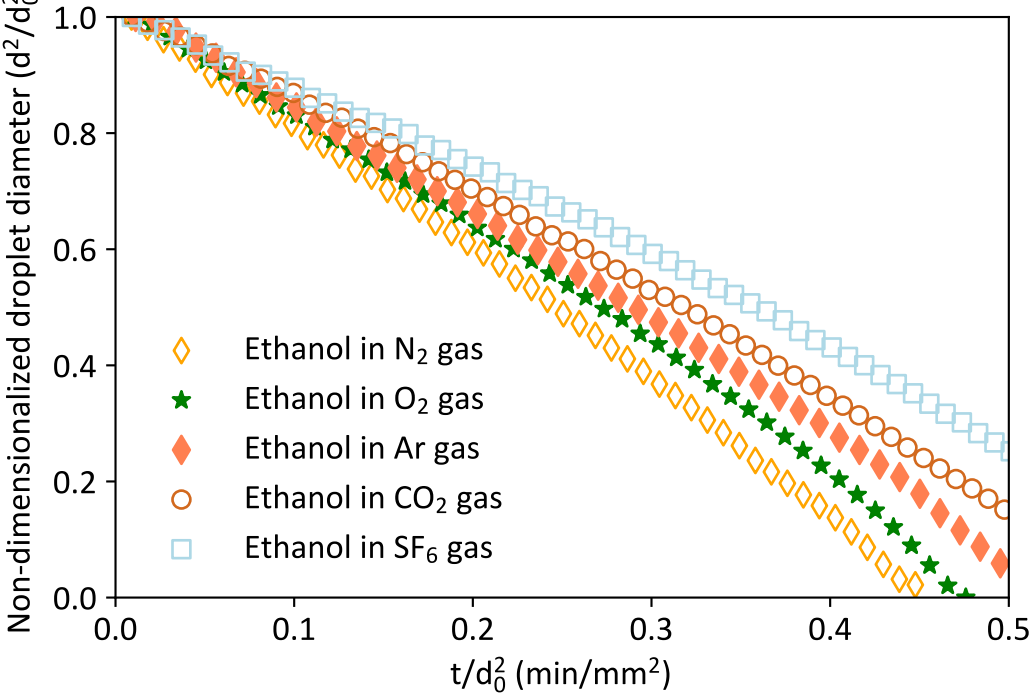
Non-dimensionalized droplet diameter (d^2/d_0^2)
1.0
0.8
0.6
0.4
0.2
0.0
0.0
0.1
0.2
0.3
0.4
0.5
t/d_0^2 (min/mm^2)
Ethanol in N_2 gas
Ethanol in O_2 gas
Ethanol in Ar gas
Ethanol in CO_2 gas
Ethanol in SF_6 gas

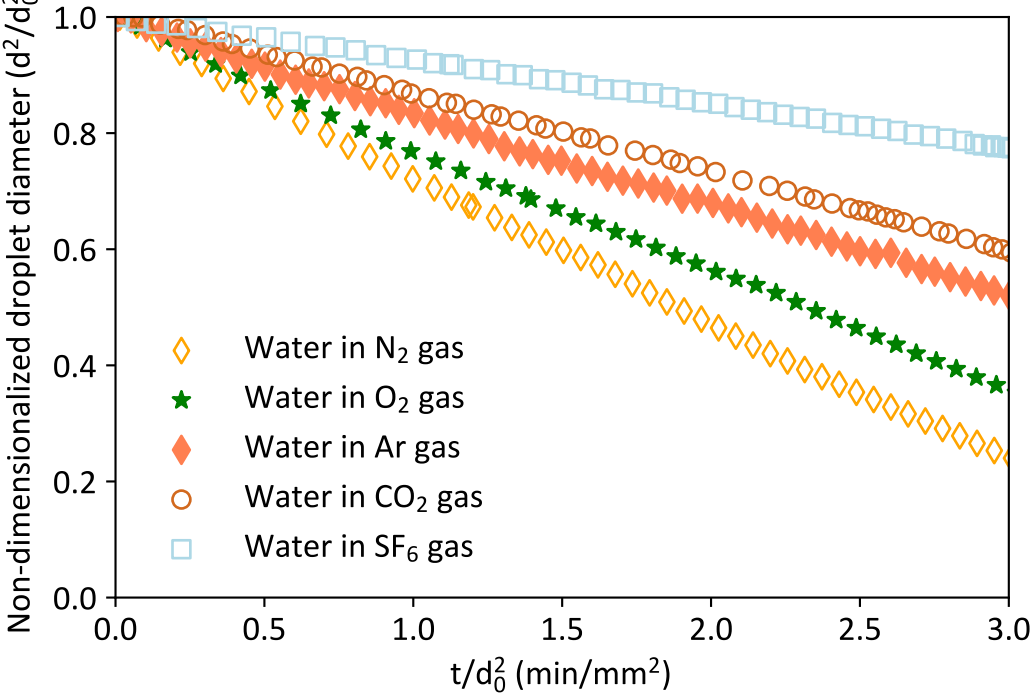
Non-dimensionalized droplet diameter (d^2/d_0^2)
1.0
0.8
0.6
0.4
0.2
0.0
0.0
0.5
1.0
1.5
2.0
2.5
3.0
t/d_0^2 (min/mm^2)
Water in N_2 gas
Water in O_2 gas
Water in Ar gas
Water in CO_2 gas
Water in SF_6 gas

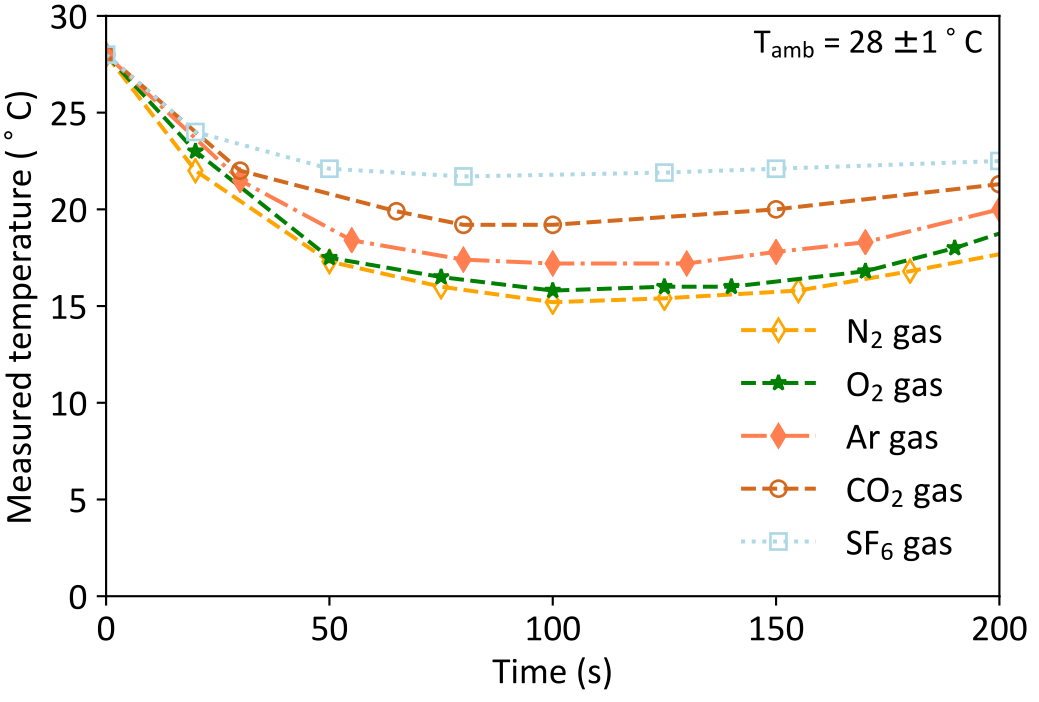
T_{amb} = 28 ±1 ° C
Measured temperature (° C)
Time (s)
0
5
10
15
20
25
30
0
50
100
150
200
N_2 gas
O_2 gas
Ar gas
CO_2 gas
SF_6 gas

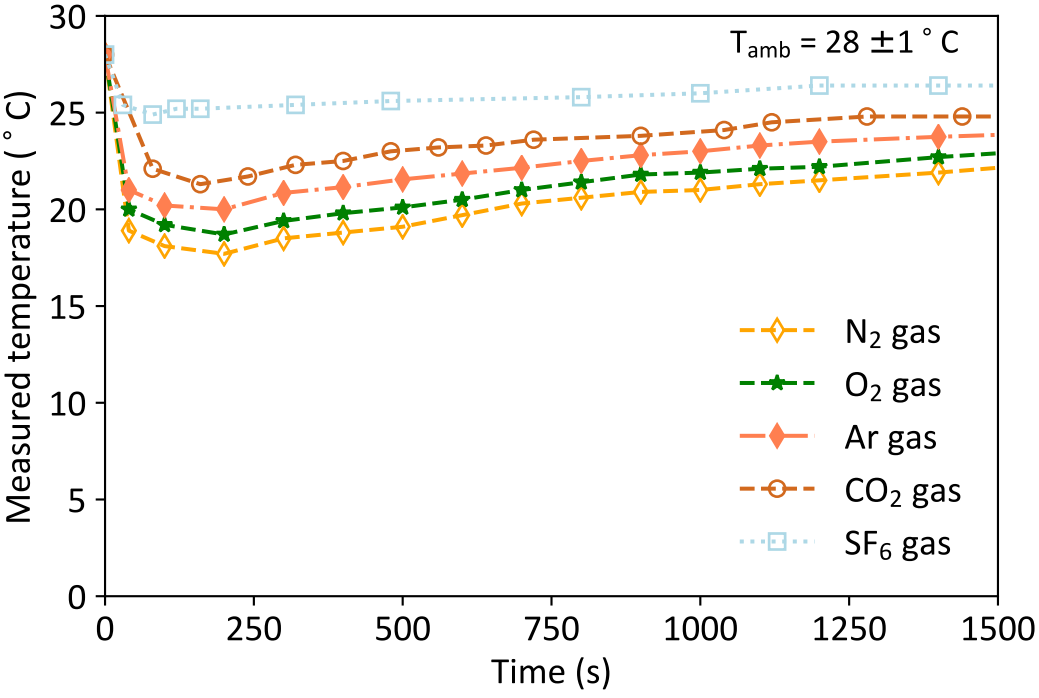
T_{amb} = 28 ±1 ˚C
Measured temperature (˚C)
Time (s)
0
5
10
15
20
25
30
0
250
500
750
1000
1250
1500
N_2 gas
O_2 gas
Ar gas
CO_2 gas
SF_6 gas

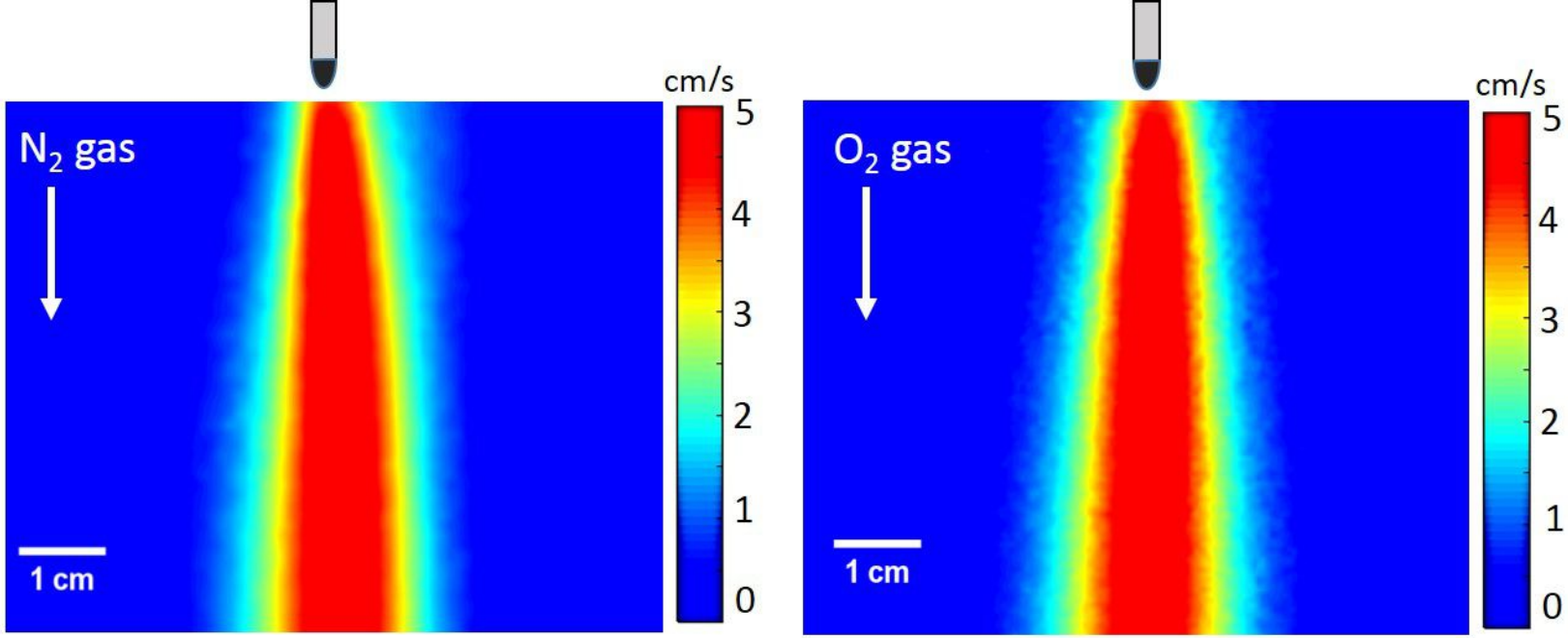

Ethanol droplets

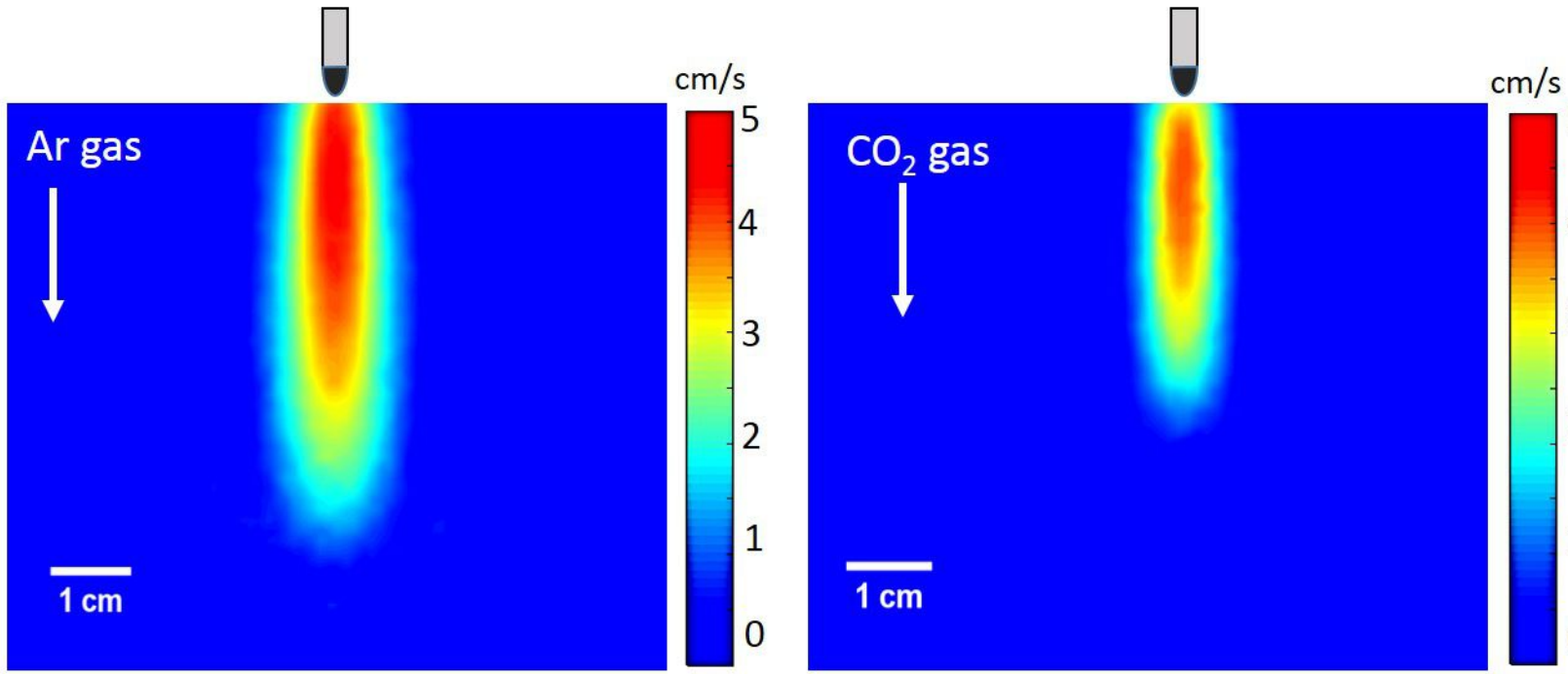

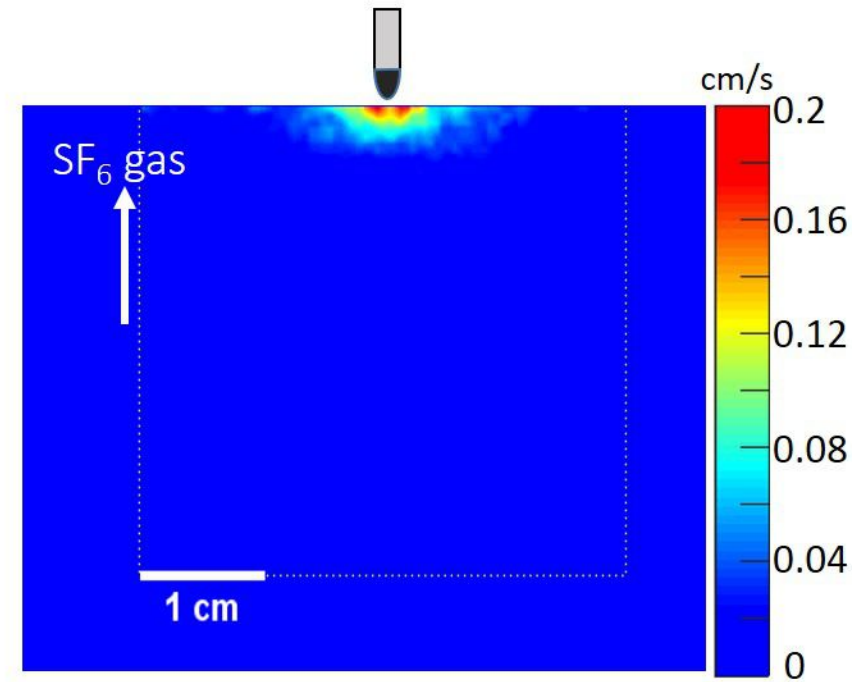

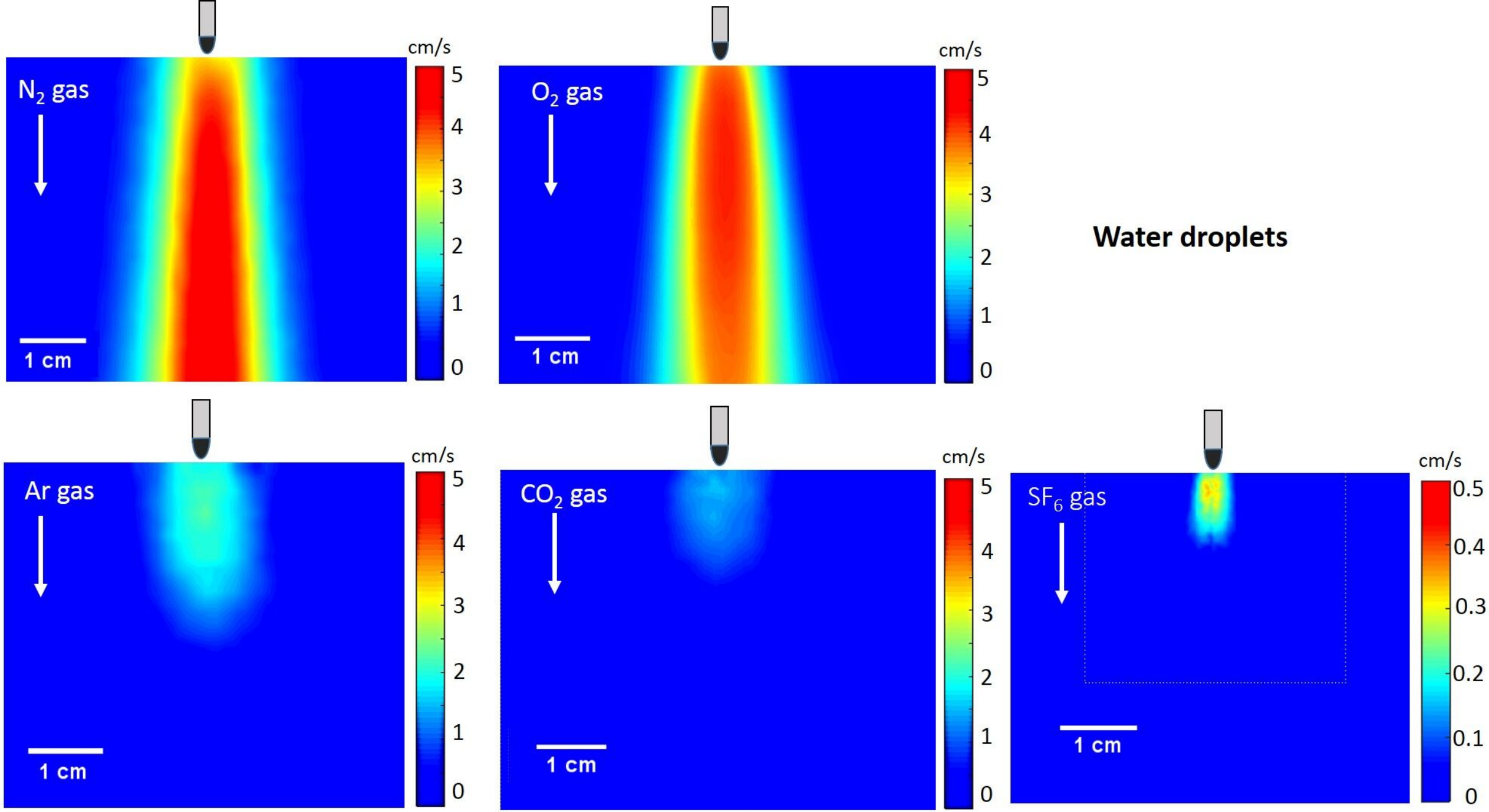
N_2 gas
1 cm
cm/s
5
4
3
2
1
0
O_2 gas
1 cm
cm/s
5
4
3
2
1
0
Water droplets
Ar gas
1 cm
cm/s
5
4
3
2
1
0
CO_2 gas
1 cm
cm/s
5
4
3
2
1
0
SF_6 gas
1 cm
cm/s
0.5
0.4
0.3
0.2
0.1
0

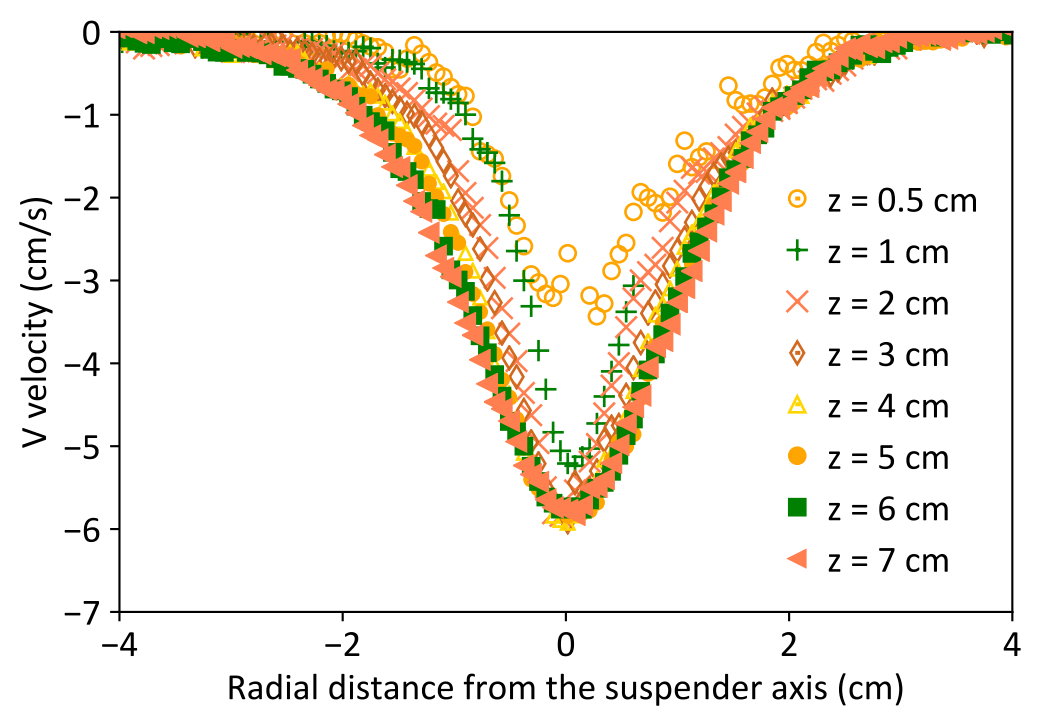
0
−1
−2
−3
−4
−5
−6
−7
V velocity (cm/s)
−4
−2
0
2
4
Radial distance from the suspender axis (cm)
z = 0.5 cm
z = 1 cm
z = 2 cm
z = 3 cm
z = 4 cm
z = 5 cm
z = 6 cm
z = 7 cm

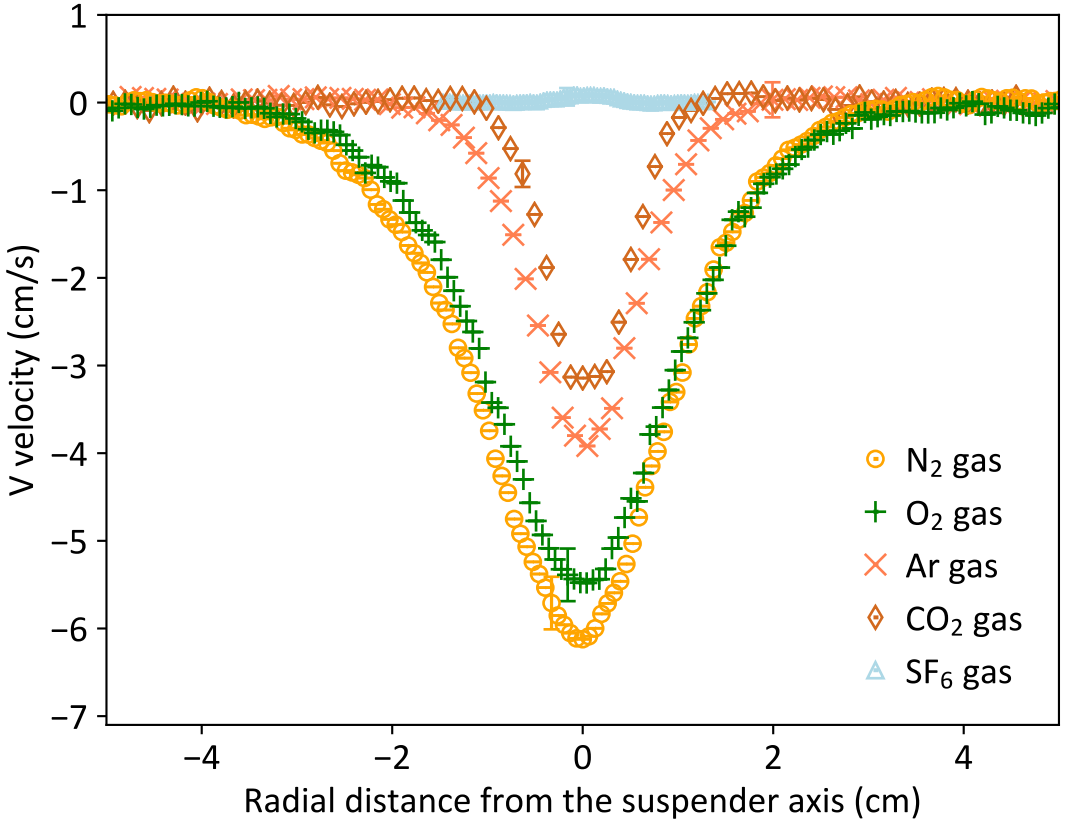
V velocity (cm/s)
Radial distance from the suspender axis (cm)
N2 gas
O2 gas
Ar gas
CO2 gas
SF6 gas

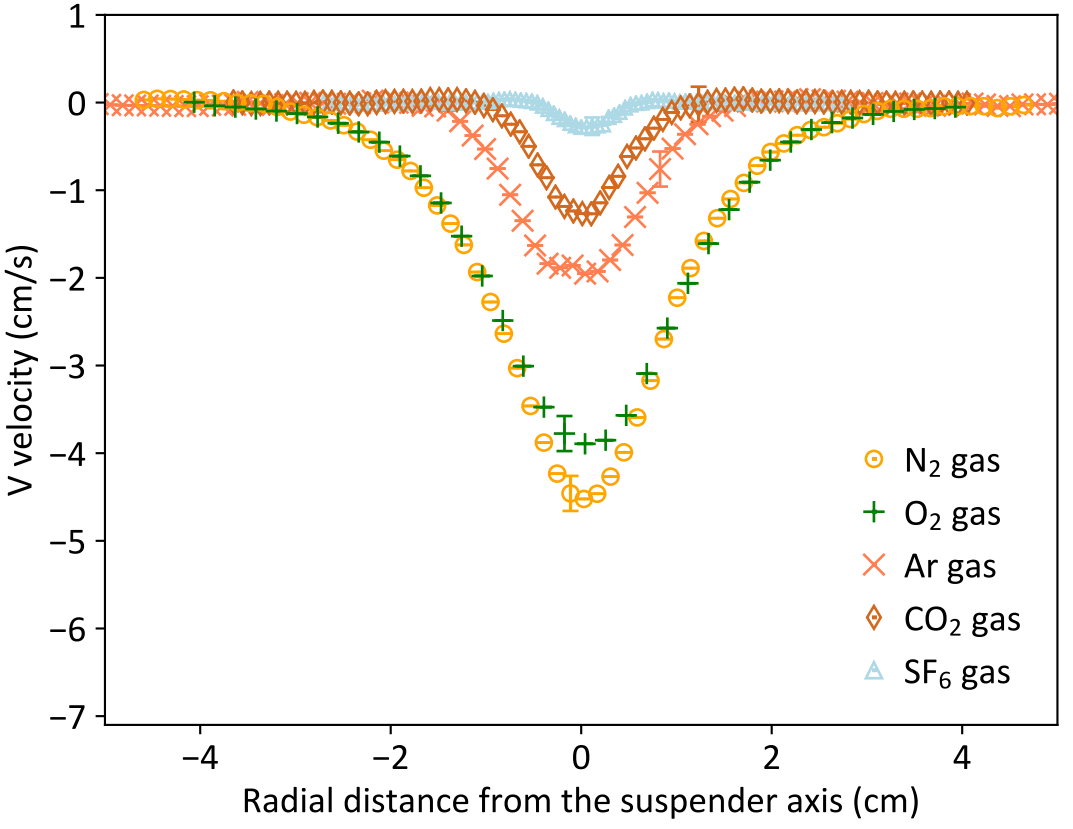
V velocity (cm/s)
Radial distance from the suspender axis (cm)
N2 gas
O2 gas
Ar gas
CO2 gas
SF6 gas

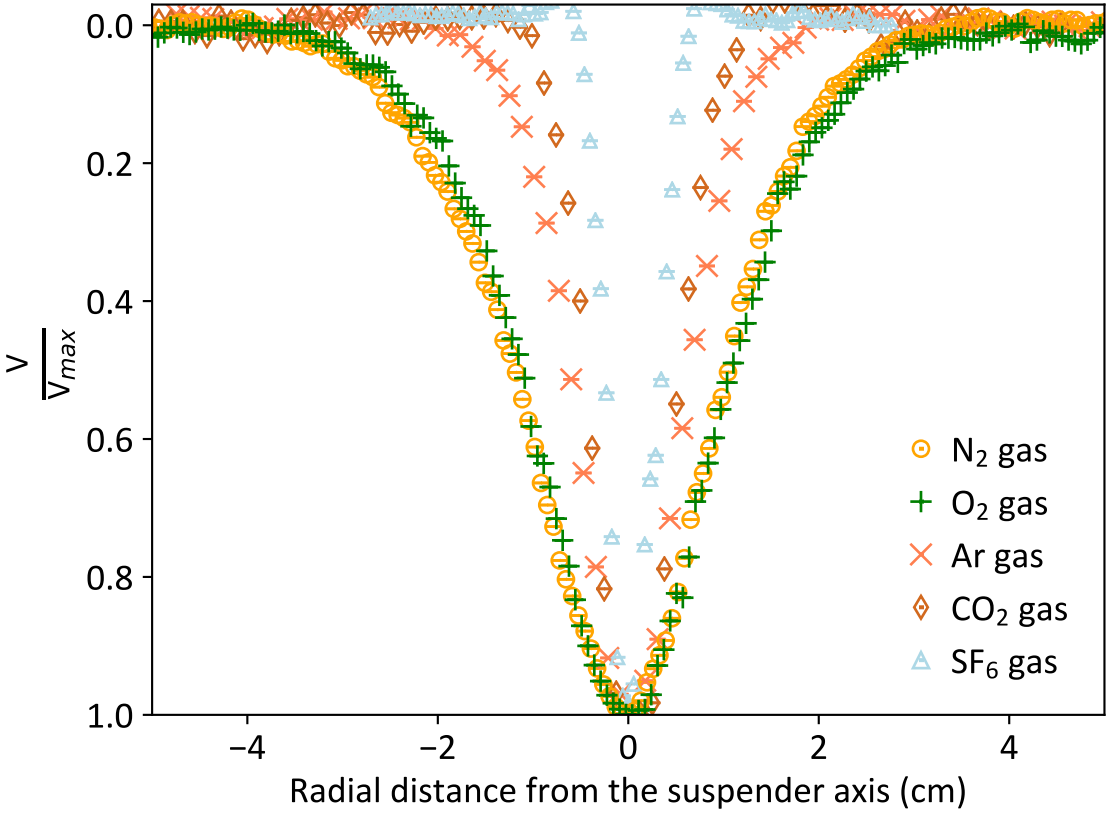
0.0
0.2
0.4
0.6
0.8
1.0
V / Vmax
−4
−2
0
2
4
Radial distance from the suspender axis (cm)
N2 gas
O2 gas
Ar gas
CO2 gas
SF6 gas

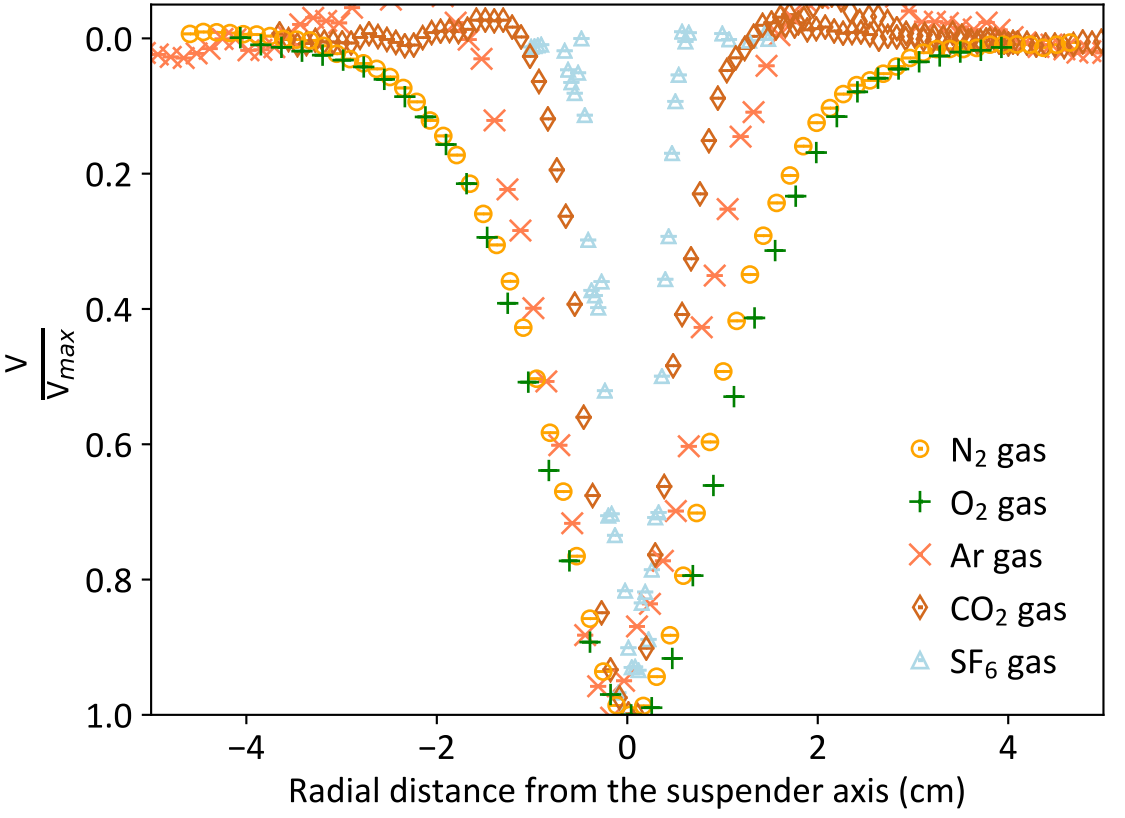
0.0
0.2
0.4
0.6
0.8
1.0
V / Vmax
−4
−2
0
2
4
Radial distance from the suspender axis (cm)
N2 gas
O2 gas
Ar gas
CO2 gas
SF6 gas

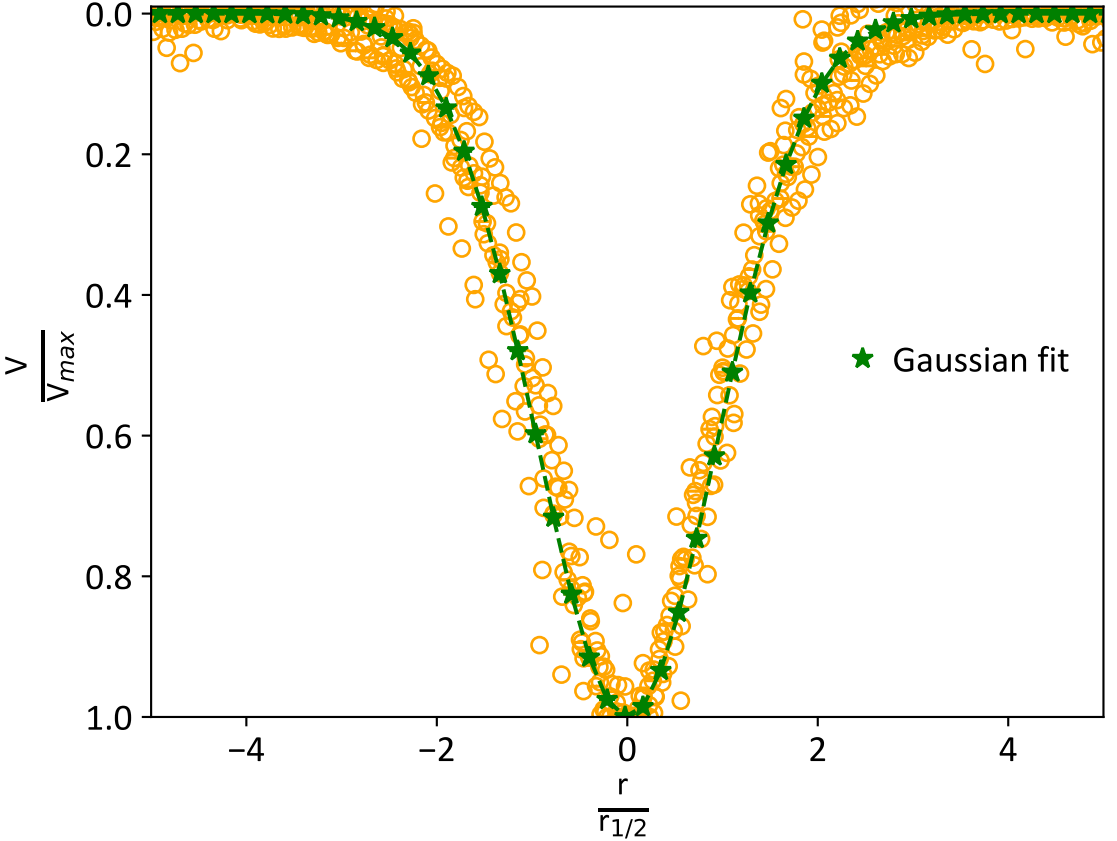
0.0
0.2
0.4
0.6
0.8
1.0
v / v_max
−4
−2
0
2
4
r / r_1/2
Gaussian fit

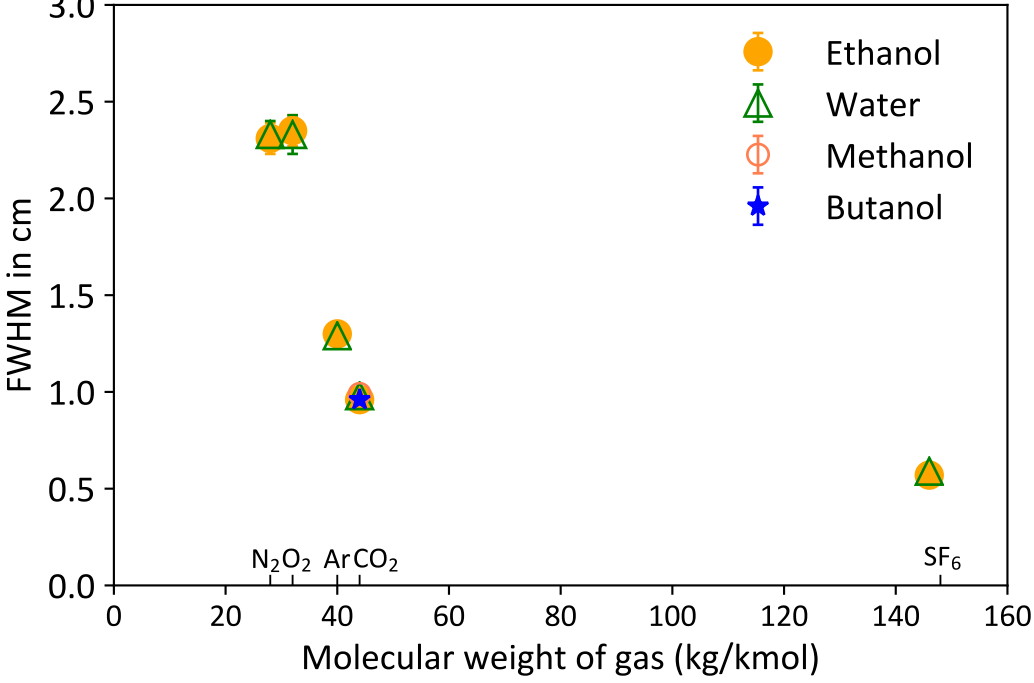
3.0
2.5
2.0
1.5
1.0
0.5
0.0
FWHM in cm
0
20
40
60
80
100
120
140
160
Molecular weight of gas (kg/kmol)
Ethanol
Water
Methanol
Butanol
N_2
O_2
Ar
CO_2
SF_6

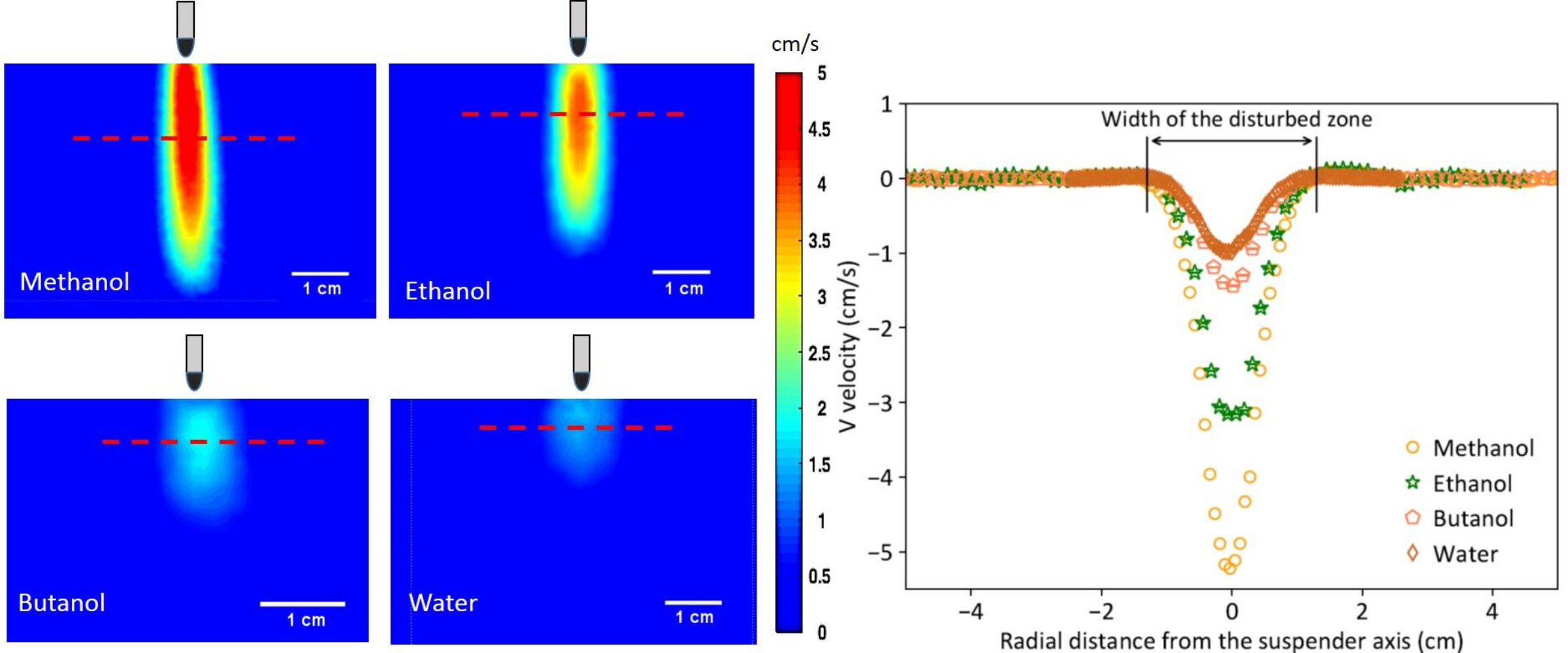
Methanol
1 cm
Ethanol
1 cm
Butanol
1 cm
Water
1 cm
cm/s
5
4.5
4
3.5
3
2.5
2
1.5
1
0.5
0
Width of the disturbed zone
V velocity (cm/s)
1
0
−1
−2
−3
−4
−5
−4
−2
0
2
4
Radial distance from the suspender axis (cm)
Methanol
Ethanol
Butanol
Water

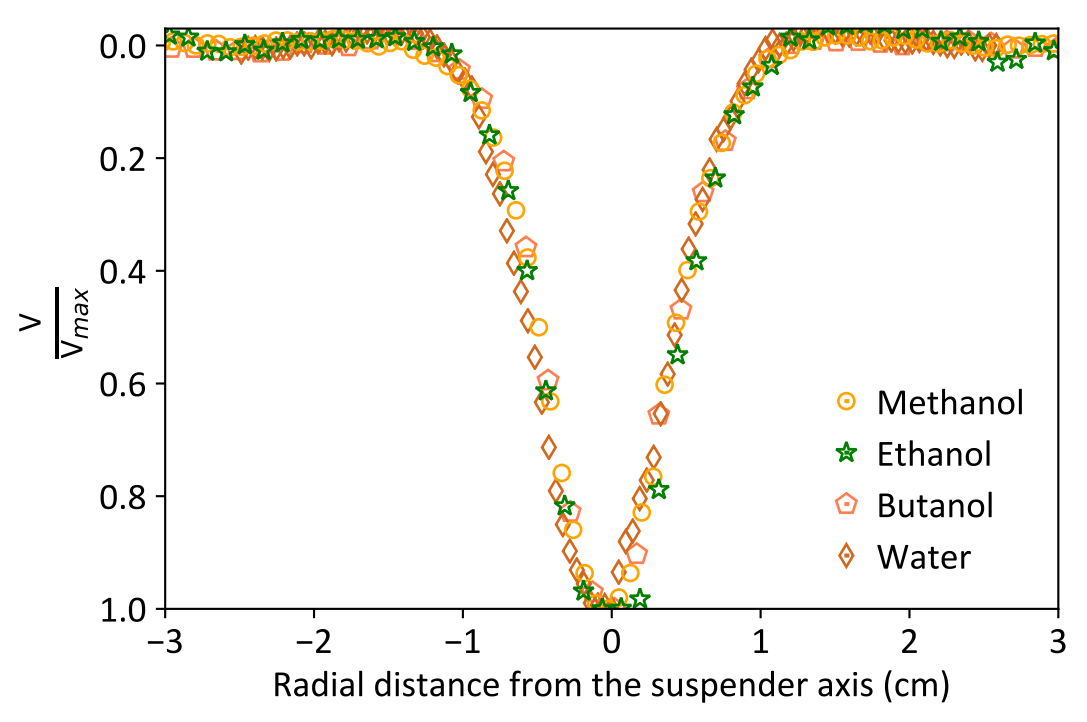
0.0
0.2
0.4
0.6
0.8
1.0
V / V_max
−3
−2
−1
0
1
2
3
Radial distance from the suspender axis (cm)
Methanol
Ethanol
Butanol
Water

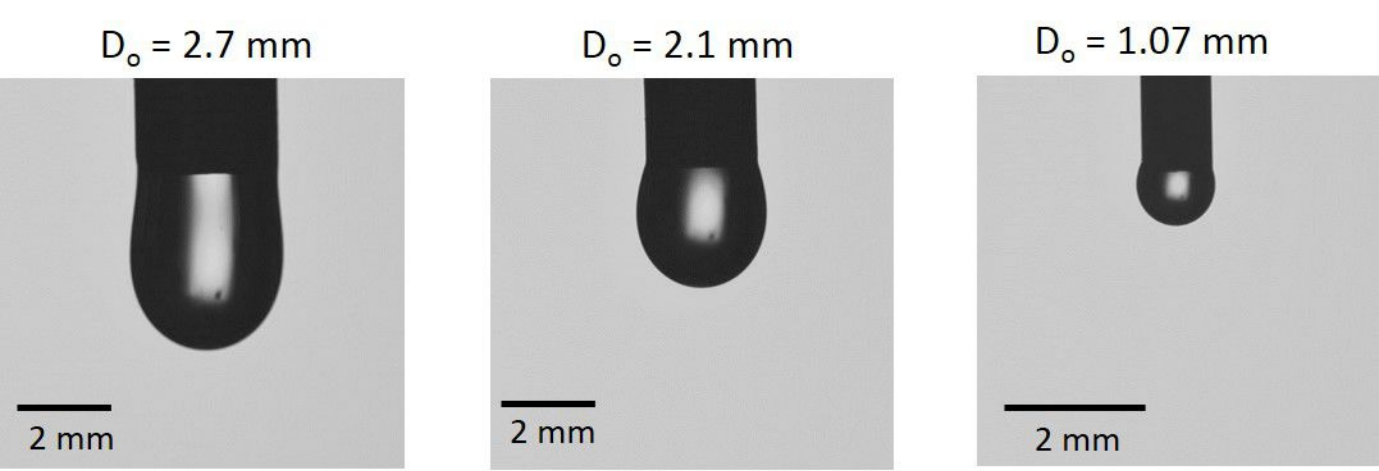
D_o = 2.7 mm
2 mm
D_o = 2.1 mm
2 mm
D_o = 1.07 mm
2 mm

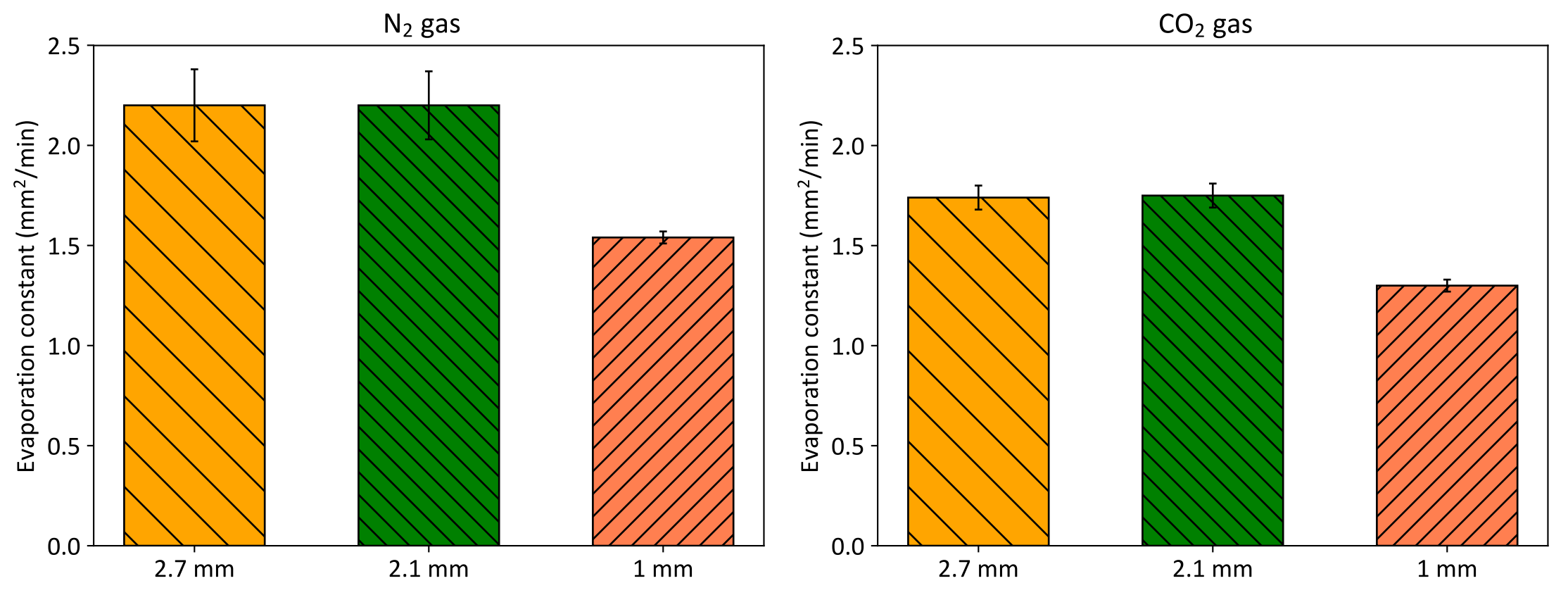
N_2 gas
CO_2 gas
Evaporation constant (mm^2/min)
0.0
0.5
1.0
1.5
2.0
2.5
2.7 mm
2.1 mm
1 mm

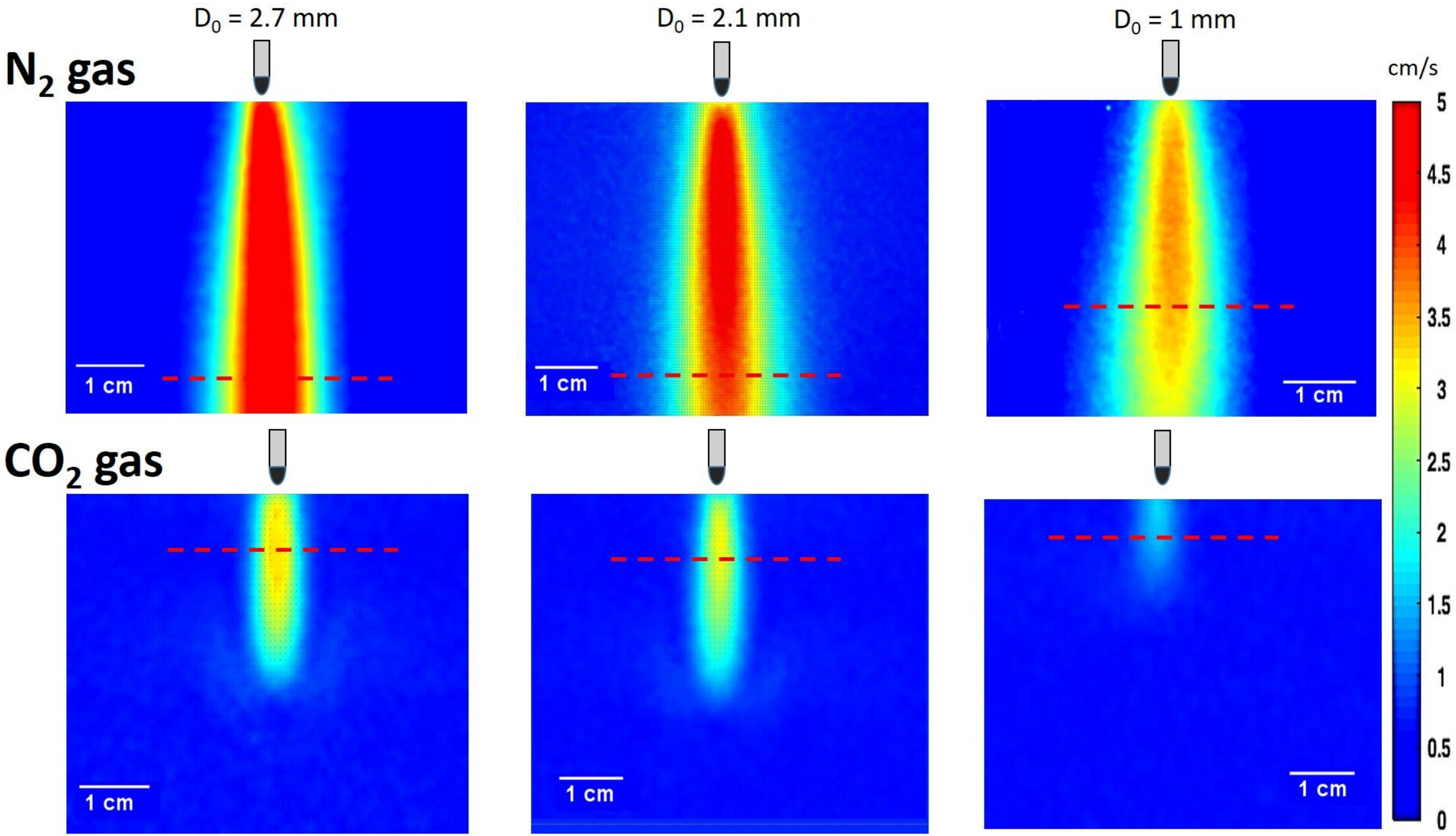
D_0 = 2.7 mm
D_0 = 2.1 mm
D_0 = 1 mm
N_2 gas
CO_2 gas
cm/s
5
4.5
4
3.5
3
2.5
2
1.5
1
0.5
0
1 cm
1 cm
1 cm
1 cm
1 cm

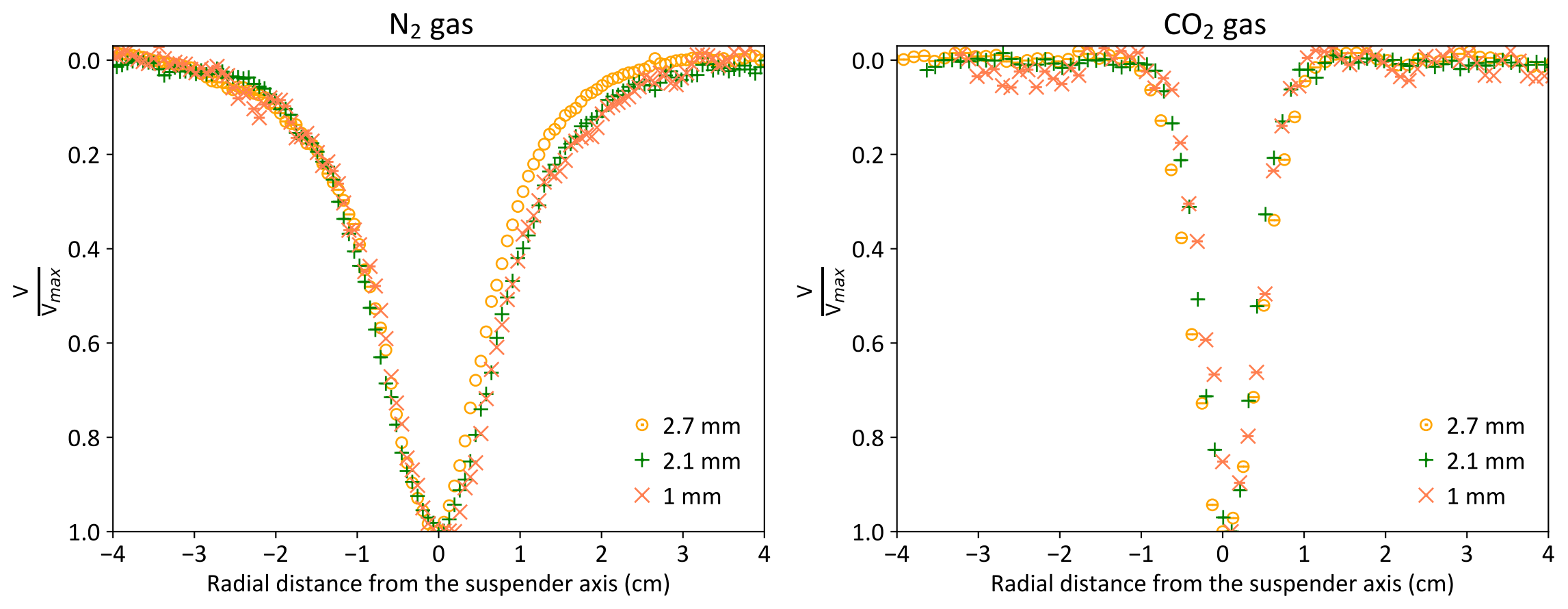
N_2 gas
CO_2 gas
$\frac{V}{V_{max}}$
0.0
0.2
0.4
0.6
0.8
1.0
−4
−3
−2
−1
0
1
2
3
4
Radial distance from the suspender axis (cm)
2.7 mm
2.1 mm
1 mm